Noname manuscript No.
(will be inserted by the editor)

Generalized Geometry Projection:

A Unified Approach for Geometric Feature Based Topology Optimization

Simone Coniglio · Joseph Morlier · Christian Gogu · Rémi Amargier

Received: date / Accepted: date

Abstract Structural topology optimization has seen many methodological advances in the past few decades. In this work we focus on continuum-based structural topology optimization and more specifically on geometric feature based approaches, also known as explicit topology optimization, in which a design is described as the assembly of simple geometric components that can change position, size and orientation in the considered design space. We first review various recent developments in explicit topology optimization. We then describe in details three of the reviewed frameworks, which are the Geometry Projection method, the Moving Morphable Components with Esartz material method and Moving Node Approach. Our main contribution then resides in the proposal of a theoretical framework, called Generalized Geometry Projection, aimed at unifying into a single formulation these three existing approaches. While analyzing the features of the proposed framework we also provide a review of smooth approximations of the maximum operator for the assembly of geometric features. In this context we propose a saturation strategy in order to solve common difficulties encountered by all reviewed approaches. We also explore the limits of our proposed strategy in terms of both simulation accuracy and optimization performance on some numerical benchmark examples. This leads us to recommendations for our proposed approach in order to attenuate common discretization induced effects that can alter optimization convergence.

Keywords Topology Optimization · Geometry Projection · Moving Morphable Components · Moving Node Approach · Smooth Geometry assembly

S.Coniglio
Airbus Operations S.A.S.
316 route de Bayonne
31060 Toulouse Cedex 09
France
Tel.: +33 (0)561937259
E-mail: simone.coniglio@airbus.com

J. Morlier
Institut Clment Ader (ICA),
CNRS, ISAE-SUPAERO, UPS,
INSA, Mines-Albi,
3 rue Caroline Aigle,
31400 Toulouse, France
E-mail: j.morlier@isae-supaero.fr

C. Gogu
Institut Clment Ader (ICA),
CNRS, ISAE-SUPAERO, UPS,
INSA, Mines-Albi,
3 rue Caroline Aigle,
31400 Toulouse, France

R. Amargier
Airbus Operations S.A.S.
316 route de Bayonne
31060 Toulouse Cedex 09
France

1 Introduction

The manufacturing industry is faced with multiple challenges in both cost reduction and product performance improvement in order to stay competitive in the market. In this context, structural optimization is a key feature for improving existing products and finding disruptive concepts. In particular, topology optimization appears quite promising in this context, as it deals with the determination of the optimal structural layout, given various performance objectives and constraints. For this reason it can be used to inspire non-conventional solutions or derive design principles for similar problems. Since the pioneering work of [5], topology optimization

has received considerable research attention. Numerous topology optimization approaches such as SIMP (Solid Isotropic Material with Penalization) approach [4,76], level set approach [1,50], and evolutionary approach [54,56] have been successfully proposed and implemented. Direct density based approaches [4,6,76], which are currently among the most popular ones, can reach organic or free form designs, defining the local presence or absence of material. In Zhu et al. [81], the interested reader can find a review of this family of approaches in the Aerospace design applications. The exploration power of these approaches, their freedom and their ease in handling large changes in the design configuration without re-meshing come however at the cost of some drawbacks as well:

- The number of design variables and of degrees of freedoms in the finite element model grows quite fast in 3D problems and their resolution becomes quickly prohibitive especially if considering optimization formulation that do not only include compliance and volume fraction.
- The typical "bionic" designs obtained with direct density based methods, even if highly effective, may not be easily compatible with manufacturing requirements (e.g. casting, rolling, overhang angle constraints, etc). Indeed as analyzed in the recent survey by Liu and Ma [30], and more recently of Liu et al. [29] the implementation of manufacturing considerations in topology optimization is still a challenging, highly active area of research.
- Intermediate densities often subsist in the final design in direct density based approaches due to computational cost constraints, preventing the full convergence towards black and white designs. The gray elements would then have to be threshold to black and white solutions, which can lead to a loss in performance compared to the optimum.
- The density formulation of the topology optimization problem is ill posed and need to be transformed into a well posed one through restriction to feasible set of solutions [7]. Some approaches like mesh independent filter techniques [41], depending on the filter size, can be computationally expensive.

An alternative family of approaches seeks to both use geometric primitives (i.e. geometric components) to define the optimal solution and inherit a fixed mesh as typical in direct density based topology optimization. In the literature one can find two major groups of approaches incorporating geometric features in topology optimization:

- A first group combines the free-form topology optimization with embedded components or holes shaped as geometric primitives. (c.f. Chen et al. [9];Qian and Ananthasuresh [38]; Xia et al. [55]; Zhang et al. [69,73]; Zhou and Wang [77]; Zhu et al. [80])
- A second group, to which this work belongs, represent the solution only by means of geometric primitives. Norato [36] provides an extensive description of works dealing with these approaches. The precursor of these methods is the bubble method (Eschenauer et al. [14]), one of the first form of topology optimization. Still this approach require re-meshing during the optimization process which affects its computational burden. Another work that can be consider as belonging to this category is the Feature-based topology optimization [11], where the structure is obtained as the results of Boolean operations over simple geometric feature structures, in this case holes. The same author proposes in [10] an implicit control of the solution quality using a quadratic term of the energy in the formulation of the optimization problem. In the work of Seo et al. [40], the solution is described using trimmed spline surfaces and the isogeometric analysis. In the Adaptive Mask Overlay Topology Synthesis Method, Saxena et al. [39] circular, rectangular or elliptical holes are considered in the solution and the structural analysis is performed on the remaining solid structure using hexagonal elements. A similar approach is applied by Wang et al. [49]: a fixed mesh is employed this time and a regularized Heaviside function is used to evaluate the mechanical properties on a fixed finite element mesh. Liu et al [31] proposed to use Compactly supported Radial basis functions to interpolate simple geometric features in a level set topology optimization framework. The performance of the resulting structure was then computed thanks to the extended finite element method (XFEM). In the ISOCOMP approach of Lin et al. [26], the simultaneous optimization of both the location of holes and the layout of material is studied with the use of both isogeometric analysis and the Hierarchical Partition of Unity Field Compositions (HPFC) theory, which is employed for both geometry and solution field approximations.

In this second family of methods, four approaches represent a solution as the union of geometric entities that can move, stretch and analytically modify their shapes: the moving morphable components (MMC) method (Guo et al. [16,17], Zhang et al. [64,71]) ; the geometry projection (GP) method (Bell et al. [3], Norato et al. [35], Zhang et al. [62]); the Method of Moving Morphable Bars (MMB) Hoang et al. [19] and the Moving Node Approach (MNA), introduced in the Master the-

sis of Overvelde [37]. We refer to these approaches as explicit topology optimization approaches, highlighting the fact that the material description is explicitly described, instead of implicitly as it is the case for direct density based approaches, where the layout is describe by a mapping of presence and absence of material. In [17], an explicit level set function is used to determine the geometry of moving morphable components with uniform thickness. The XFEM approach was employed as an alternative for the displacement computation [24,48,53]. The same framework is also presented in Zhang et al. [72] where MMC is identified as a way of extending techniques commonly employed in shape optimization, with the freedom inherited from topology optimization. Moving components with variable thickness are used in [71], and the esartz material model is employed to enhance computational efficiency. In the work of Zhang et al. [65] length scale control is achieved by directly controlling the component's minimal thickness. In Deng et al. [12] the MMC approach is successfully implemented to solve various types of problems, like the design of compliant mechanisms and of low-frequency resonating micro devices. In the work of Zhang et al. [64], the MMC framework is extended to 3D structures. The complexity of the solution is controlled in [74] by controlling the maximum number of components in the final solutions.

The Moving Morphable Voids approach [63] makes use of b-splined shaped holes, explicitly piloted in the topology optimization. The proposed framework, not only reduce the optimization burden due to variables reduction, but also impacts the cost of the evaluation of the displacement field, eliminating the element completely contained in the void region from the analysis. The same framework is applied to tackle stress based topology optimization in [66]. In Zhang et al. [70] the control of the solution is achieved by varying explicitly the boundaries of Components or voids using B-spline curves. In Takalloozadeh et al. [47] the topological derivative is implemented in the MMC approach. In the work of [18] the ability of MMC to determined self supported structures is studied and in Liu et al. [27] the MMCs/MMVs framework is employed to determine graded lattice structures achievable with additive layer manufacturing technologies. In Hou et al. [20] the MMC framework is proposed based on Isogeoemtric Analysis (IGA) instead of finite element analysis (FEA). In Zhang et al. [68], the MMC approach is employed to design multi-material structures and in Zhang et al. [67] it is employed to find the best layout of stiffening ribs including buckling constraints. Geometric non-linearities are considered in Zhu et al. [79] for MMC and in Xue et al. [57] for MMV. In Lei et al. [25] machine learning techniques like: support vector regression (SVR) [42] and the K-nearest-neighbors (KNN) [2], were adopted in order to speed up the resolution of the optimization problem, under MMC framework. In Liu et al. [28] an efficient strategy is proposed to decouple the finite element mesh discretization from the discretization employed to assemble the stiffness matrix on the basis of the geometric configuration. In Sun et al. [43] the topology optimization of a 3D multi-body systems considering large deformations and large overall motion is achieved using MMC.
With the Method of Moving Morphable Bars (MMB) Hoang et al. [19] introduce round ended bars in the topology optimization framework that can overlap and change both shape and position. As main features of this work one can identify the control of both minimal and maximal thickness of the components, the use of sigmoid Heaviside function to project the components on the fixed finite element mesh, the use of SIMP material model to penalize intermediate density and the boolean union of components realized making the product of Heaviside functions. MMB was also studied in wang et al. [51] for the layout of planar multi-component systems.
The Geometry Projection (GP) approach was initially introduced by Norato et al. [34], for the shape optimization of holes over a fixed finite element mesh. This basic idea was developed further by Bell et al. [3] to make the topology optimization of structures composed by rectangular components in 2D, by Norato et al. [33] using 2D round ended bar components that can both overlap and merge. The same author proposed to use this approach to find the best distribution of short fiber reinforcement in [35]. In Zhang et al. [62] Geometry projection approach was implemented for 3D solid structures composed of rectangular plates. In Zhang et al. [58] stress based topology optimization is conducted on 2D topology optimization problems, using GP. The design of unit cells for lattice materials in 3D is considered in Watts et al. [52]. In Zhang et al. [59] curved plates are considered as building blocks of 3D topology optimization problems using GP. In Zhang et al. [60] Geometry Projection was employed to design the rib reinforcement of plates in 3D. In the work of Norato [36] supershapes geometric features are employed as building blocks in a 2D topology optimization framework based on geometry projection. In Kazemi et al. [21], the Geometry Projection was applied to multi-material design of 2D and 3D structures. In Zhang et al. [61] a tunneling strategy is proposed to alleviate the initial point dependency in Geometry projection.

It is clear that the domain of explicit topology optimization is currently a very active area of research.

We chose to focus in this paper on the following three frameworks, which follow different approaches for achieving explicit topology optimization: the Moving Morphable Components (MMC) with Esartz material approach, the Geometry Projection (GP) approach and Moving Node Approach (MNA). The main goal of this paper is to propose a generalized theory, that we call Generalized Geometry Projection (GGP), of which all three approaches can be seen as particular cases. A further contribution resides in the proposal of a specific saturation strategy, that can be adopted to overcome the difficulties that can be encountered in the assembly of geometric features, required in all considered explicit topology optimization approaches. Finally, a root cause of optimization convergence difficulties is extensively analyzed and possible solutions to circumvent this issue are discussed.

The remainder of this paper is structured as follows: Section 2 first introduces the geometric description of the components employed in this work and the common steps undertaken by all three reviewed topology optimization approaches. We then review Moving Morphable Components (MMC) with Esartz material, Geometry Projection (GP) and Moving Node Approach (MNA) in subsections 2.1, 2.2 and 2.3 respectively. The proposed Generalized Geometry Projection that unifies all three approaches is presented in subsection 2.4. The techniques employed to obtain the geometric assembly are reviewed in subsection 2.5 and the sensitivity chain is detailed in subsection 2.6 with the aim of providing practical implementation recommendations. A benchmark problem is then considered in section 3: the parametric study of a cantilever beam is conducted in subsection 3.1 and the topology optimization of a short cantilever beam is solved in subsection 3.2. Discussion of the results and final recommendations are provided in section 4. Finally, conclusions and future work perspectives are outlined in section 5.

2 Methods

In this section we first describe three of the existing 2D explicit topology optimization approaches: Moving Morphable Components (MMC) with Esartz material model; Geometry Projection (GP); Moving Node Approach (MNA). Then we describe the proposed method: Generalized Geometry Projection (GGP), aimed at unifying into a single formulation these three existing approaches. To simplify the equations we will consider the same geometric components proposed in Norato et al. [35] for all reviewed approaches c.f. figure 1a. This component is defined by five geometric parameters defining the position of the center of the component $\{X, Y\}$, the components dimensions $\{L, h\}$ and the component's orientation $\{\theta\}$. The final topology will then be described as a superposition of multiple such basic components. In this section we will refer to ω as the area occupied by a geometric component and to $\partial\omega$ as its boundary. If more than one component is used to describe the area occupied by material, then we will refer to ω_i and to $\partial\omega_i$ as the i^{th} component's area and boundary respectively. We will refer to ω and to $\partial\omega$ as area and boundary of the union of all components i ($\omega = \cup_{i=1}^{n}\omega_i$). In order to define explicitly the con-

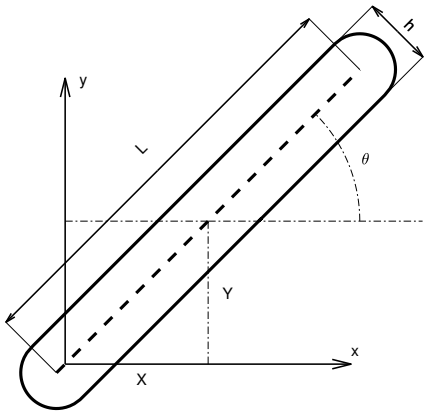

(a)

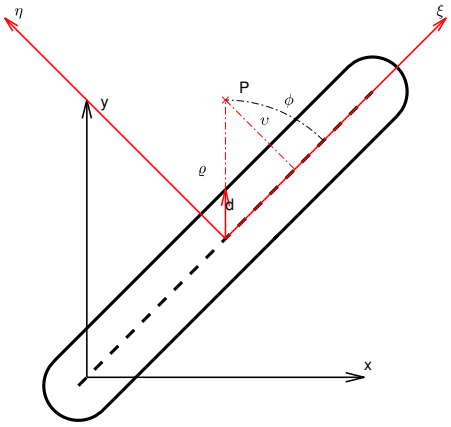

(b)

Fig. 1: Geometric primitive (i.e. basic geometric component) used for all the reviewed methods. (a) The explicit geometric parameters associated to the component are $\{X, Y, L, h, \theta\}$. (b) Plot defining the local polar coordinates $\{\varrho, \phi\}^T$, the distance from the component boundary d, and the distance from the component middle axis υ

tour of this component, we introduce polar coordinates $\{\varrho, \phi\}^T$ as defined in figure 1b. We refer to d as the radial distance of the component's center $\{X, Y\}^T$ from the component boundary $\partial\omega$ that can be computed as a function of the angle ϕ and of the component sizes L and h as:

$$d(\phi, L, h) = \begin{cases} \sqrt{\frac{h^2}{4} - \frac{L^2 \sin\phi^2}{4}} + \frac{L}{2}|\cos\phi| & \text{if } \cos\phi^2 \geq \frac{L^2}{L^2+h^2}, \\ \frac{h}{2|\sin\phi|} & \text{otherwise.} \end{cases} \quad (1)$$

This piece-wise definition is at least of class $\mathbf{C}^1(\mathbb{R})$. Given a point $\{X_g\} \equiv \{x, y\}^T \in \mathbb{R}^2$, its polar coordinates can be defined as:

$$\varrho(x, y, X, Y) = \sqrt{(x-X)^2 + (y-Y)^2} \quad (2)$$

$$\phi(x, y, X, Y, \theta) = \begin{cases} \arctan\left(\frac{y-Y}{x-X}\right) - \theta & \text{if } x \neq X, \\ \frac{\pi}{2}\text{sign}(y-Y) - \theta & \text{if } x = X. \end{cases} \quad (3)$$

A consequence of the above definitions we have:

$$\{X_g\} \in \omega \cup \partial\omega \Leftrightarrow d(\phi, L, h) \geq \varrho(x, y, X, Y) \quad (4)$$

Another way of describing the same component is by the use of the signed distance as described in Norato et al. [35]:

$$\varsigma(\upsilon, h) := \upsilon - \frac{h}{2} \quad (5)$$

where υ is the distance from a point $\{X_g\} \in \mathbb{R}^2$ to the component medial axis, which can be further expressed as a function of $\{X_g\}$'s polar coordinates:

$$\upsilon(\varrho, \phi, L, h) = \begin{cases} \sqrt{\varrho^2 + \frac{L^2}{4} - \varrho L|\cos\phi|} & \text{if } \varrho^2\cos\phi^2 \geq \frac{L^2}{4}, \\ \varrho|\sin\phi| & \text{otherwise} \end{cases} \quad (6)$$

Accordingly,

$$\{X_g\} \in \omega \cup \partial\omega \Leftrightarrow \varsigma(\upsilon, h) \leq 0 \quad (7)$$

The structural model used during the topology optimization will then be described by n components, each involving following six[1] design variables $\{x_i\} = \{X_i, Y_i, L_i, h_i, \theta_i, m_i\}^T$. For the whole structure involving n components the structural performance will thus depend on $6n$ design variables denoted as vector $\{x\}$:

$$\{x\} = \begin{Bmatrix} \{x_1\} \\ \{x_2\} \\ \vdots \\ \{x_n\} \end{Bmatrix} \quad (8)$$

[1] additional variable m_i is introduced in the geometry projection approach to make a component vanish in the same way as it is done in density based approaches.

Each of the reviewed methods has its own way of updating the structural model that is used to evaluate the performance of a given design. A common feature is the fact that a linear elastic-static finite element model is employed. Here a structured uniform mesh based on $dx \times dx$ solid elements in plane stress is adopted, where dx is the element x and y size. The Poisson ratio ν and the thickness t in the out of plane direction considered to be a constant over all the design domain D. The Young's modulus E depends on the fact that the considered point belongs or not to ω. A common assumption is that the Young's modulus is piece-wise uniform over each element. For this reason, the elementary stiffness matrices $[K^{el}]$ are all of the same form i.e:

$$[K^{el}] = E^{el}[K_0] \qquad el = 1, 2, ..., N \quad (9)$$

where E^{el} is the Young's modulus of the el^{th} element, $[K_0]$ is the 8×8 stiffness matrix of a $dx \times dx$ 2D solid element in plane stress condition with thickness $t = 1$ and N is the total number of elements in the structural model. Using classic finite element theory, one can assembly the global stiffness matrix $[K]$:

$$[K] = \bigoplus_{el=1}^{N} [K^{el}] \quad (10)$$

This is used to write the static balance equation in terms of the free degrees of freedoms $\{U\}$ as:

$$[K]\{U\} = \{F\} \quad (11)$$

where $\{F\}$ is the external loads vector. If the boundary conditions are at least isostatic and $E^{el} \geq E_{min} > 0$, then the system of equation $[K]$ is non-singular and the system of equation (11) can be solved to find the displacement vector $\{U\}$.

$$\{U\} = [K]^{-1}\{F\} \quad (12)$$

In many topology optimization formulations the mass of the structure is also of interest, which is usually considered in terms of the volume fraction V associated to a given structural design layout (since V is proportional to the mass of a solution for a homogeneous material). To compute this volume fraction V the local density ρ^{el} are determined based on the design vector $\{x\}$ as will be presented in details in the next subsections for each approach.

As an example of a topology optimization formulation within this framework we provide in eq. (13) the classical formulation consisting in minimizing the compliance of the structure (i.e. maximizing its stiffness)

subjected to a volume fraction constraint and design space constraints:

$$\begin{cases} \min_{\{x\}} C = \{U\}^T\{F\} \\ s.t. \\ V = \frac{\sum_{el=1}^{N} \rho^{el}}{N} \leq V_0 \\ \{l_b\} \leq \{x\} \leq \{u_b\} \end{cases} \tag{13}$$

Where $\{l_b\}$ and $\{u_b\}$ are respectively the vectors of lower bound and upper bound for the design variables and V_0 is the maximum allowed volume fraction in the final solution.

2.1 Moving Morphable Components (MMC) with Esartz material model

In this section we review the moving morphable components (MMC) method (Guo et al. [16,17]). MMC inherits from the level set method [1] a Topology Description Function (TDF), that is positive inside the area occupied by the union of all components ω, equal to zero on the boundary $\partial\omega$ of the component and negative outside the component. The TDF values are then used either to apply the XFEM [53] on the boundaries of the components either to compute the element stiffness matrix using ersatz material model [71]. In this paper will focus on the application of the latter. The reader must note that we made some minor modifications to the original formulation, in order to include the round ended bar components (cf. Fig. 1a) with uniform thickness. The structural topology description is obtained using a topology description function (TDF), denoted χ, that satisfies following relations:

$$\begin{cases} \chi > 0 & \text{if } \{X_g\} \in \omega, \\ \chi = 0 & \text{if } \{X_g\} \in \partial\omega, \\ \chi < 0 & \text{if } \{X_g\} \in D\backslash\omega. \end{cases} \tag{14}$$

where D represents the total area of the design domain (full and voids). When more than one component is considered, the TDF of each component, denoted as $\chi_i = \chi_i(\{X_g\})$, is defined $\forall i = 1, .., n$ such that:

$$\begin{cases} \chi_i > 0 & \text{if } \{X_g\} \in \omega_i, \\ \chi_i = 0 & \text{if } \{X_g\} \in \partial\omega_i, \\ \chi_i < 0 & \text{if } \{X_g\} \in D\backslash\omega_i. \end{cases} \tag{15}$$

Since $\omega = \cup_{i=1}^{n}\omega_i$ one can verify that $\chi = \max_i \chi_i$ satisfies the conditions (14). Given a component described by the geometric variables $\{X_i, Y_i, L_i, h_i, \theta_i\}$ we have several choice for defining the TDF $\chi_i(\{X_g\})$. Here we consider the following relationship, which has the advantage of allowing simple derivations:

$$\chi_i = 1 - \left(\frac{4v_i^2}{h_i^2}\right)^{\alpha} \quad \text{with } \alpha \geq 1 \tag{16}$$

Figure 2 illustrates the contour plot of the TDF χ_i contour of the generic component of figure 1a.

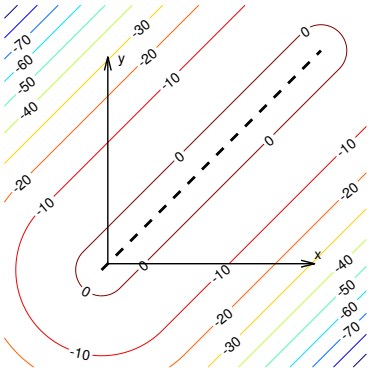

Fig. 2: $\chi(\{X_g\})$ contour plot of the generic component of figure 1a. We considered $\alpha = 1$, $X = 1$, $Y = 1$, $L = 3$, $h = 0.5$, $\theta = \frac{\pi}{4}$. The domain D of the plot is $[-1, 2.5] \times [-1, 2.5]$

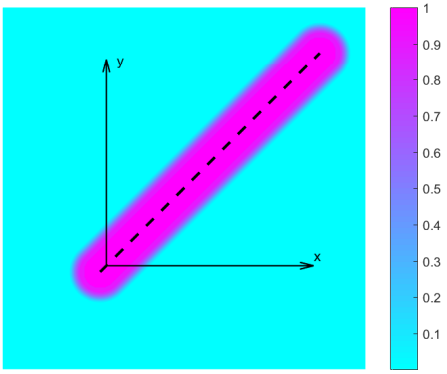

Fig. 3: $H_\epsilon(\chi(\{X_g\}))$ filled contour plot of the component in figure 1a. We considered $\alpha = 1$, $X = 1$, $Y = 1$, $L = 3$, $h = 0.5$, $\theta = \frac{\pi}{4}$, $\beta = 0.01$, $\epsilon = 0.6$. The domain D of the plot is $[-1, 2.5] \times [-1, 2.5]$

The presence or absence of material in the design under consideration can be obtained by the Heaviside function $H(x)$, applied to the topology description function of the union of all the components χ. In order to

have a regular behavior of the optimization problem responses, the Heaviside function $H(x)$ is replaced by a regularized version $H_\epsilon(x)$:

$$H_\epsilon(x) = \begin{cases} 1, & \text{if } x > \epsilon, \\ \frac{3(1-\beta)}{4}\left(\frac{x}{\epsilon} - \frac{x^3}{3\epsilon^3}\right) + \frac{1+\beta}{2} & \text{if } -\epsilon \leq x \leq \epsilon, \\ \beta & \text{otherwise.} \end{cases} \tag{17}$$

Where $0 < \epsilon < 1$ is a parameter that controls the amplitude of the transition between the minimum value of β ($0 < \beta << 1$) and 1. The same generic component is used in figure 3 to plot $H_\epsilon(\chi(\{X_g\}))$. One can observe that the smooth variation, from a value of 1 inside the component to a value of β outside it, is localized in a small transition zone, denoted D_g, that can be determined using equations (16)-(17):

$$D_g^{MMC} = \left\{ \{X_g\} \;\middle|\; \frac{h}{2}(1-\epsilon)^{\frac{1}{2\alpha}} \leq \upsilon \leq \frac{h}{2}(1+\epsilon)^{\frac{1}{2\alpha}} \right\} \tag{18}$$

The width of this transition zone is denoted by w_g:

$$w_g^{MMC} = \frac{h}{2}\left[(1+\epsilon)^{\frac{1}{2\alpha}} - (1-\epsilon)^{\frac{1}{2\alpha}}\right] \tag{19}$$

A peculiarity of MMC is that the width of the transition zone is directly proportional to the the component's thickness h. A direct consequence is that smaller components will have faster variation between full material and voids. The effect of this behaviour on the ill conditioning of the optimization problem will be investigated on numerical examples in the implementation section.

According to [15], the value of the Young's modulus in the el^{th}-element is considered to be:

$$E^{el} = \frac{E\left(\sum_{j=1}^{4}(H_\epsilon(\chi_j^{el}))^q\right)}{4} \tag{20}$$

Where $\chi_i^{el}, i = 1, ..., 4$ are the values of the TDF at the four nodes of the element el and q is a parameters that has the role of penalization, in order to render the variation of Young's modulus even faster at the boundary of the component. In figure 4a, the single component example of figure 1a has been used to plot the distribution of Young's modulus according to equation (20) over a 50×50 finite element mesh. In order to obtain the local density ρ^{el}, which was not explicitly considered in [71], an equivalent expression that leads to the same value of volume fraction for the same configuration is proposed here:

$$\rho^{el} = \frac{\sum_{j=1}^{4}(H_\epsilon(\chi_j^{el}))}{4} \tag{21}$$

In figure 4c the corresponding distribution of ρ^{el} is also represented. Figures 4c and 4a look very similar except for the transition on element boundary that is faster for the Young's modulus plot due to the effect of the penalization parameter q.

2.2 Geometry Projection (GP)

In this section we review the approach proposed by Norato et al. [35]. Geometric projection first computes the signed distance between each element central point and each component surface. The element local volume fraction is then computed by the mean of a spherical sampling window centred in the element centroid. Density and Young's modulus in the element are computed as function of the volume fraction of the sampling window that is occupied by material. The density coming from each component is unified using the maximum function or its smooth approximation [23]. The solution is described by the union of geometric primitives such as the one in figure 1a. To update model densities the geometry projection method is employed [34]. A circular sampling window $\mathbf{B}_P^r$ of radius r is considered around the el^{th}-element center $\left\{X_g^{el}\right\}$ c.f. figure 5. The local volume fraction δ^{el} is simply given by the fraction of the window that is filled with material:

$$\delta_i^{el} = \frac{|\mathbf{B}_P^r \cap \omega_i|}{|\mathbf{B}_P^r|} \tag{22}$$

where $|\cdot|$ denotes the measure of the area. The denominator can be computed analytically as the area of the circle $|\mathbf{B}_P^r| = \pi r^2$. The numerator of equation (22) on the other hand is more complex but can be approximately computed with the assumption that r is small enough. In this case the restriction of $\partial\omega$ to the circle $\mathbf{B}_P^r$ can be considered as a straight line. As a consequence one can compute:

$$\delta_i^{el} \approx \begin{cases} 0 & \text{if } \varsigma > r, \\ \frac{1}{\pi r^2}\left[r^2 \arccos\left(\frac{\varsigma}{r}\right) - \varsigma\sqrt{r^2-\varsigma^2}\right] & \text{if } -r \leq \varsigma \leq r, \\ 1 & \text{otherwise.} \end{cases} \tag{23}$$

Where the signed distance ς (cf. eq. (5)) is computed in the el^{th} element centroid $\left\{X_g^{el}\right\}$ and with respect to the i^{th} component. In order to avoid stiffness matrix singularities, the local densities are modified as follows.

$$\tilde{\delta}_i^{el} = \delta_{min} + (1 - \delta_{min})\delta_i^{el} \tag{24}$$

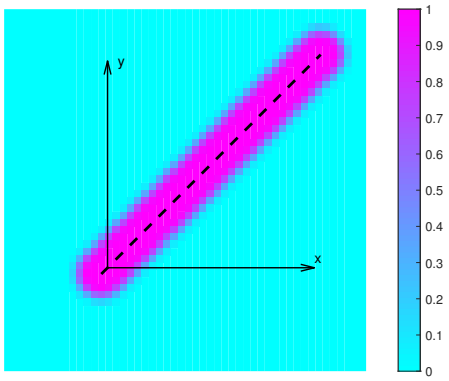

(a) $\frac{E^{el}}{E}$

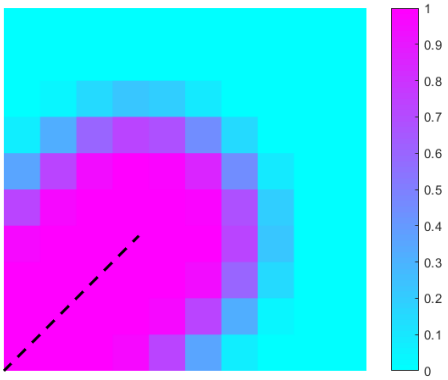

(b) $\frac{E^{el}}{E}$ zoom on the component boundary.

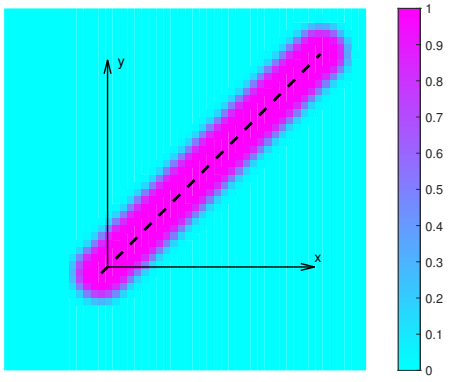

(c) ρ^{el}

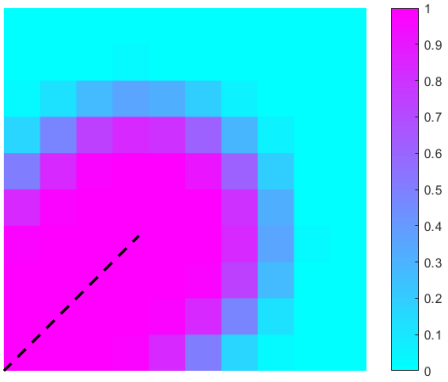

(d) ρ^{el} zoom on the component boundary.

Fig. 4: Distribution of $\frac{E^{el}}{E}$ (a-b) and ρ^{el} (c-d) for the generic component of figure 1a and for a 50×50 FE mesh over the domain of X_g. The same parameters of figure 3 are also considered here with $q = 2$.

where δ_{min} is the minimum of local volume fraction to be considered in the analysis. Moreover:

$$\hat{\delta}_i^{el}(m_i, \gamma) = \tilde{\delta}_i^{el} m_i^{\gamma} \tag{25}$$

Where m_i is the i^{th} component mass or out of plane thickness [35] and $\gamma \geq 1$ penalizes the intermediate value of the component's mass. The local densities are finally computed by taking the union of all the components using a smooth approximation of the maximum function:

$$\rho^{el}(\gamma_v, \kappa) = \Pi(\{\hat{\delta}^{el}(\{m\}, \gamma_v)\}, \kappa) \tag{26}$$

where κ is an aggregation constant and $\{\hat{\delta}^{el}(\{m\}, \gamma_v)\}$ is the vector of local density stemming from each component. Here we do not specify the form of the smooth approximation of the maximum function Π, which will be investigated in details in the implementation section.

In order to determine the value of the Young's modulus of an element, the following equation is used which involves a second penalty parameter $\gamma_c > \gamma_v$

$$E^{el} = \rho^{el}(\gamma_c, \kappa) E \tag{27}$$

This penalization is very similar to the one adopted by the SIMP approach and is effective in order to progressively eliminate a component with an intermediate value of m_i throughout the optimization iterations [35]. In figure 6, the generic component of figure 1a is considered to show the distribution of both Young's modulus and element densities over a 50×50 mesh. Note again that the transition zone from full material to void is concentrated on the boundary of the component:

$$D_g^{GP} = \left\{ \{X_g\} \;\middle|\; \frac{h}{2} - r \leq \upsilon \leq \frac{h}{2} + r \right\} \tag{28}$$

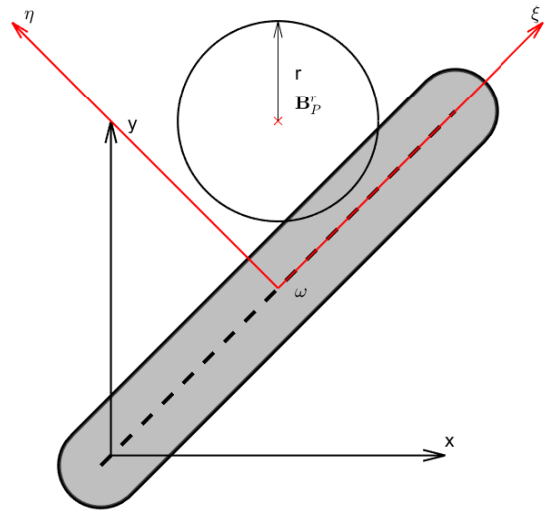

Fig. 5: Basic component and notations associated to the Geometry Projection method [35]

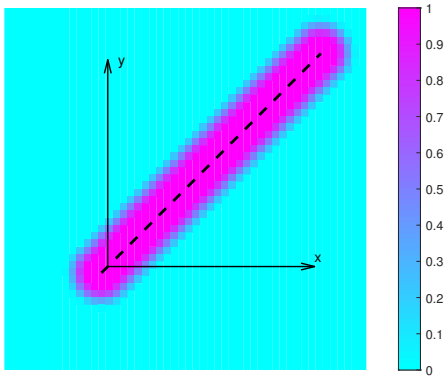

Fig. 6: Distribution of $\frac{E^{el}}{E}$ for the generic component of figure 1a and for a 50×50 mesh over the domain of X_g. We considered $X = 1, Y = 1, L = 3, h = 0.5, \theta = \frac{\pi}{4}, \gamma_c = 3, r = 0.105, \delta_{min} = 10^{-6}$. Due to the choice of $m = 1$ the same distribution is obtained for ρ^{el}.

As a consequence this time the thickness of the transition zone is:

$$w_g^{GP} = 2r \tag{29}$$

This thickness does not depend on the component size h. In order to achieve regular density distributions, h will need to be greater or equal than $2r$. To delete inactive components, variable m can still be used within the optimization algorithm.

2.3 Moving Node Approach (MNA)

Overvelde [37], proposed in his master's thesis an alternative flow-inspired topology optimization approach, the Moving Node Approach (MNA). For this approach, the building blocks of a solution are defined as mass nodes. Each element's center position is recomputed with respect to a local coordinate system in each component center . Then weighting functions are directly applied to the local variable to compute the component local density contribution. In order to compute the union between the components, this time, the densities are summed. Since the sum can be greater than one, to keep the resulting density bounded from 1 an adapted procedure was proposed in [37] called asymptotic density. Another peculiarity of Overvelde work was the fact of using either Finte Element Analysis or meshless method (cf. [32]) for the displacement evaluation. The idea was to reduce both design variable and degrees of freedom number, using the mass nodes for both the geometric description and the solution displacement. Unfortunately in [37] the gain in dofs number was compensated by the stiffness matrix cost (both in memory and elapsed time) and by its ill conditioning where the mass nodes reached each other. The update of the finite element model is done by operating through weighting functions w that are driven by the geometry of each component. In this paper we considered a modified weighting function with respect to [37] in order to consider round ended bar components. For the mass node of figure 1a one can write:

$$w(v, h, \varepsilon) = \begin{cases} 1 & \text{if} \quad v \leq l, \\ a_3 v^3 + a_2 v^2 + a_1 v + a_0 & \text{if} \quad l < v < u, \\ 0 & \text{otherwise.} \end{cases} \tag{30}$$

Where

$$l = \frac{h}{2} - \frac{\varepsilon}{2} \tag{31}$$

$$u = \frac{h}{2} + \frac{\varepsilon}{2} \tag{32}$$

$$a_3 = \frac{2}{\varepsilon^3} \tag{33}$$

$$a_2 = -\frac{3h}{\varepsilon^3} \tag{34}$$

$$a_1 = 3\frac{(h^2 - \varepsilon^2)}{\varepsilon^3} \tag{35}$$

$$a_0 = -\frac{(h+\varepsilon)^2(h-2\varepsilon)}{4\varepsilon^3} \tag{36}$$

$$\tag{37}$$

The local density can then be computed as:

$$\delta_i^{el} = m_i^{\gamma} w(v_i^{el}, h_i, \varepsilon_i) = m_i^{\gamma} w_i^{el} \tag{38}$$

Where we call v_i^{el} the distance from the el^{th} element centroid $\{X_g^{el}\}$ to the i^{th} component middle axis computed using equation (6). To make the union of all mass nodes a smooth approximation of the maximum function is again typically employed:

$$\rho^{el} = \Pi(\{\delta\}_v^{el}, \kappa) \tag{39}$$

Finally the Young's modulus is updated using a power law:

$$E^{el} = E_{min} + (E - E_{min})(\Pi(\{\delta\}_c^{el}, \kappa))^{p_b} \tag{40}$$

Where $p_b \geq 1$ is used to penalize intermediate densities. In figures 7a,7c both Young's modulus distribution and densities are considered for the same generic component and same mesh as for figures 4a,4c and 6. Note that in this case as well the gray region is localized in the transition zone defined this time by:

$$D_g^{MNA} = \left\{ \{X_g\} \;\middle|\; \frac{h-\varepsilon}{2} \leq v \leq \frac{h+\varepsilon}{2} \right\} \tag{41}$$

The thickness of this transition zone is then defined as:

$$w_g^{MNA} = \varepsilon \tag{42}$$

This thickness is, as for Geometry Projection, independent from the component thickness h. On the other hand one can observe in figure 7a, compared to Geometry Projection, the effect of the penalty $p_b > 1$ that reduces the value of the densities in the transition zone.

2.4 Generalized Geometry Projection

In this subsection we introduce the proposed Generalized Geometry Projection method as a generalization of the Geometry Projection (Bell et al. [3]; Norato et al. [35]; Zhang et al. [62]). Moreover we will show that the proposed approach can recover all the reviewed approaches in terms of relationships between the geometric configuration and finite element model update. Essentially, all reviewed approaches can be seen as a particular case of the proposed Generalized Geometry Projection method. Let us first formalize the general procedure that is common to all existing explicit approaches c.f. fig8. The first step consists in choosing the geometric primitives, i.e. the building blocks that are going to be used to build the solution through Boolean operations. As for all reviewed approaches, round ended bar components (cf. fig. 1a) in a 2D design space will be considered here as geometric primitive. Then, characteristic functions Υ have to be defined for each geometric primitive i. A characteristic function can be defined for the set of points inside the geometric primitive ω_i as:

$$\Upsilon(\{X_g\}, \omega_i) = \begin{cases} 1 & \text{if} \quad \{X_g\} \in \omega_i \\ 0 & \text{otherwise.} \end{cases} \tag{43}$$

For implementation purpose (in order to improve the regularity of the functions in the optimization problem), $W_i(\{X_g\}, \{X_i\}, \{r\})$ should be chosen to be a regular approximation of
$\Upsilon(\{X_g\}, \omega_i)$. Accordingly, for the choice of a characteristic function we require here :

$$\begin{cases} 0 \leq W_i(\{X_g\}, \{X_i\}, \{r\}) \leq 1 \\ \lim_{r \to \lambda} \left(W_i(\{X_g\}, \{X_i\}, \{r\}) \right) = \Upsilon(\{X_g\}, \omega_i) \\ W_i(\{X_g\}, \{X_i\}, \{r\}) \in \mathbf{C}^1(\mathbb{R}^{d_g}) \end{cases} \tag{44}$$

where d_g is the dimension of the $\{X_g\}$ space (in the present case $d_g = 2$, since we only consider 2D problems) and $\lambda \in \{0, +\infty\}$. The vector of hyper-parameters $\{r\}$ will control the length scale of the transition of W_i between 0 and 1. We will also require the functions W_i to be non increasing with respect to any direction that points outward of the component. For a more formal definition, we introduce the following procedure: given a point $\{X_g\} \in \mathbb{R}^{d_g}$, one can find its projection on the geometric feature boundary as: $\{X_g^\star\} = \arg\min_{\{x\} \in \partial\omega_i} \| \{x\} - \{X_g\} \|$. One can then find the outward direction in $\{X_g^\star\}$ defined as $\{n^\star\}$. Finally we impose for any $\{X_g\}$ that:

$$\left\{ \frac{\partial W_i(\{X_g\}, \{X_i\}, \{r\})}{\partial X_g} \right\}^T \{n^\star\} \leq 0 \tag{45}$$

This condition avoids useless difficulties in optimization due to component border non-monotonicity.
As aforementioned, a great virtue of all reviewed approaches consists in using a unique finite element model to simulate each configuration, thus avoiding re-meshing. In the proposed approach we also propose a procedure to update a given finite element model based on the configuration of the various components. In order to do so, the third step of Fig. 8 consists in using a procedure that transforms the continuous distribution of material represented by $W_i(\{X_g\}, \{X_i\}, \{r\})$ into a piece-wise uniform distribution of Young's modulus and density inside each element of the FE mesh. The geometry projection proposed by Norato et al. [34] is here generalized to consider several sampling window shapes.[2]

[2] Here we consider only $dx \times dx$ uniform meshes, but the presented framework is also valid for non uniform and irregular mesh. Moreover, note that the sampling window shape can eventually be shaped as the finite element mesh considering a slightly different formula in the sampling window definition that we won't detail here for conciseness.

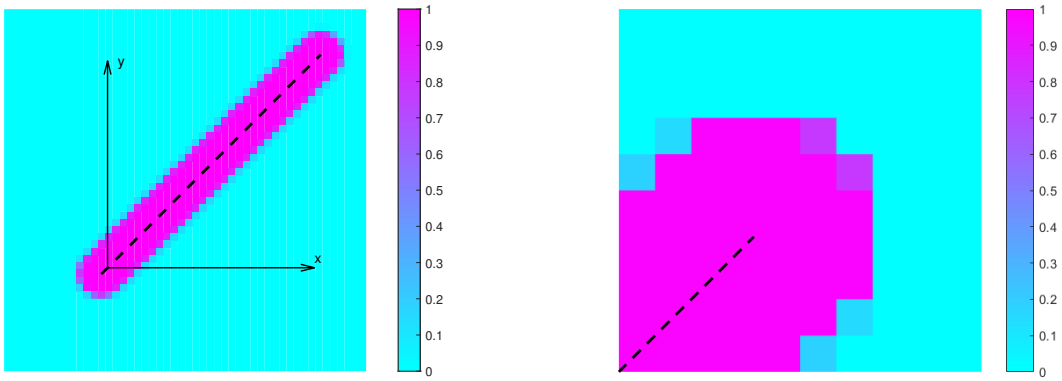

(a) $\frac{E^{el}}{E}$ (b) $\frac{E^{el}}{E}$ zoom on the component boundary

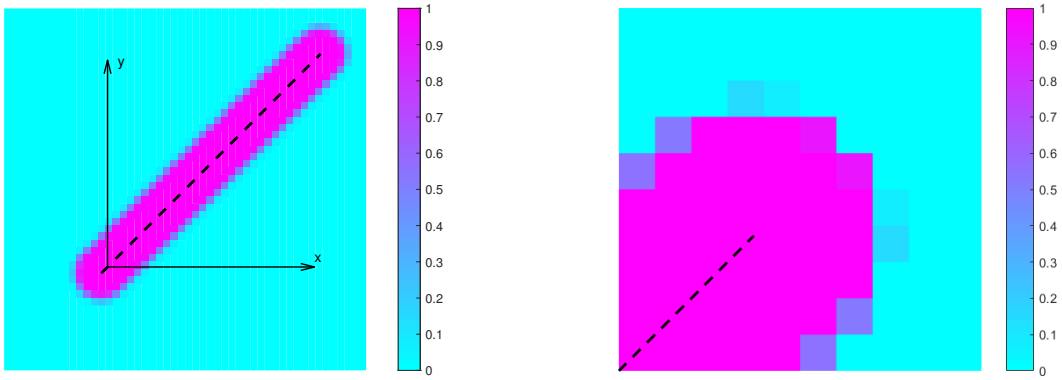

(c) ρ^{el} (d) ρ^{el} zoom on the component boundary

Fig. 7: Distribution of$\frac{E^{el}}{E}$ (a-b) and ρ^{el} (c-d) for the generic component of figure 1a and for a 50×50 FE mesh over the domain of X_g. We considered $X = 1, Y = 1, L = 3, h = 0.5, \theta = \frac{\pi}{4}, \gamma = 3, \varepsilon = 0.14, p_b = 3, E_{min} = 10^{-6}$.

For this purpose we consider the following definition of the sampling window:

$$\mathbf{D}(\{X_g\}, p, R) = \{\{X\} \in \mathbb{R}^{d_g} \mid \| \{X\} - \{X_g\} \|_{2p} \leq R\} \tag{46}$$

Next, we introduce a formulation for the local density in each element of the FE mesh that we propose in the generalized geometric projection method:

$$\delta_i^{el}(W_i, p, R) = \frac{\int_{\mathbf{D}(\{X_g^{el}\}, p, R)} W_i(\{X\}, \{X_i\}, \{r\}) d\Omega}{\int_{\mathbf{D}(\{X_g^{el}\}, p, R)} d\Omega} \tag{47}$$

This formulation can be seen as a weighted volume fraction estimation over the sampling window.

The evaluation of this expression can be done for example by Gauss quadrature:

$$\delta_i^{el} \approx \frac{\sum_{k=1}^{N_{gp}} \psi_k W_{ik}}{\sum_{k=1}^{N_{gp}} \psi_k} \tag{48}$$

where W_{ik} are the values of characteristic functions in Gauss point locations and ψ_k are the integration weights. One must note that the characteristic function has not to be the same for Young's Modulus and density models. We refer to $\{\delta^{el}\}_v$ as the vector of local volume fractions computed in the el^{th} element centroids for each component in the optimization using density characteristic function denoted as W^v. In the same way we refer to $\{\delta^{el}\}_c$ as the vector of local volume fraction computed in the el^{th} element centroid for each component in the optimization using density characteristic function denoted as W^c. Finally the last step in the

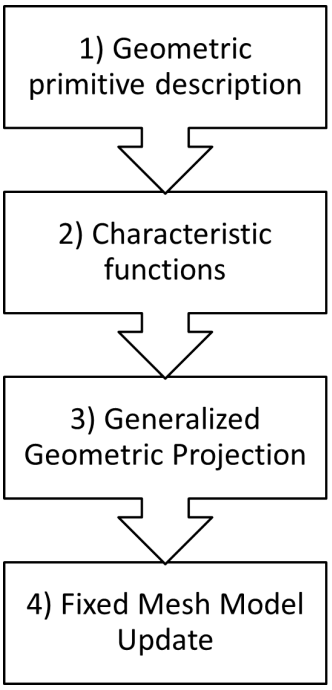

Fig. 8: General procedure employed by explicit approaches. In step 1) Geometric primitives are chosen, so that their layout, shape and sizes can be explicitly driven by the optimization procedure. In step 2) According to the geometry description characteristic functions has to be defined for each feature and for all material properties. These will be computed in each sampling window gauss points. In step 3) Generalized Geometry Projection is used to compute the value of local volume fraction for all material properties. Finally in step 4) the Finite element model is updated according to the value of each local volume fraction in each element centroid.

general procedure of figure 8 consists in updating the fixed mesh of the FE model using:

$$E^{el} = \mathbb{M}(\{\delta^{el}\}_c, E, E_{min}, \kappa) \tag{49}$$

$$\rho^{el} = \mathbb{V}(\{\delta^{el}\}_v, \kappa) \tag{50}$$

Where $\mathbb{M}$ and $\mathbb{V}$ are regular functions that link respectively the Young's modulus and local densities in each finite element to the local volume fraction values δ^{el} stemming from each geometric primitive. [3] We will now show that all three reviewed approaches can be recovered as a particular case by the Generalized Geometry Projection approach.

[3] As a special case one could assemble geometric primitives before computing the local volume fractions. In this case the vectors of local volume fraction reduces to scalars computed that are unchanged by geometric assembly.

Let's consider the example of MMC with Esartz material model[4]. Let's consider $W^v = H(\chi)$,$W^c = (H(\chi))^q$, $p \to \infty$ and $R = \frac{\sqrt{3}}{2}dx$. Let's consider Gauss-Legendre numerical integration in the sampling window, that for $p \to \infty$, is $D \equiv [-R, R] \times [-R, R]$. We considering 2×2 Gauss points for the numerical evaluation of the integral of equation (47). For the function providing the element's Young's modulus we consider:

$$\mathbb{M}(\delta^{el}, E, E_{min}) = \lim_{p\to\infty} \delta^{el}(W^c, p, R)E_0 \tag{51}$$

Given these assumptions we obtain the volume over a sampling window as:

$$\lim_{p\to\infty} \int_{\mathbf{D}(\{X_g\},p,\frac{\sqrt{3}}{2}dx)} d\Omega = \sum_{j=1}^{4} \left(\frac{\sqrt{3}}{2}dx\right)^2 = 3dx^2 \tag{52}$$

Furthermore, given the choice of 4 Gauss points, the integration involved in the calculation of the local volume fraction of eq. 47 becomes:

$$\lim_{p\to\infty} \delta^{el}(W^c, p, R) \approx \approx \frac{\frac{3}{4}dx^2 \sum_{j=1}^{4} W^c(\mathbf{x}_j)}{3dx^2} = \frac{\sum_{j=1}^{4}(H(\chi(\mathbf{x}_j)))^q}{4} \tag{53}$$

Accordingly the element's density can be expressed as:

$$\rho^{el} = \mathbb{V}(\delta^{el}(W^v, p, R), \kappa) = = \lim_{p\to\infty} \delta^{el}(W^v, p, R) \approx \frac{\sum_{j=1}^{4} H(\chi(\mathbf{x}_j))}{4} \tag{54}$$

These expressions for the Young Modulus and density are the same as those employed by the MMC method with Esartz material, meaning that the Generalized Geometric Projection approach could effectively recover it.

To recover the Geometric Projection formulation, one can consider $p = 1$ and a generic $R = r$. For these values the sampling window becomes a circular sampling window, i.e. $\mathbf{D} \equiv \mathbf{B_p}^r$. Moreover selecting $W_i = \Upsilon_i$ by the use of equation (47) with the same assumption, i.e. the restriction of $\partial\omega_i$ to be considered as straight (Bell et al. [3]; Norato et al. [35]; Zhang et al. [62]) one can find the expression of the local volume fraction $\{\delta^{el}\}$.[5] In order to compute local densities we

[4] This demonstration only applys to the case of $dx \times dx$ uniform meshes. The same demonstration can be easily extended to $dx \times dy$ uniform meshes simply changing sampling window definition. For the general situation of non uniform irregular meshes, to recover the MMC formulation one should define local sampling window shapes and a more elastic numerical integration scheme based on triangulation.

[5] The reader can note that the same result can also be obtained selecting $p \to \infty$, 1 Gauss point, $R = \frac{1}{2}dx$ and $W_i^{el} = \delta_i^{el}$ of equation (23).

set:

$$\rho^{el} = \mathbb{V}(\{\delta\}^{el}, \kappa) = \Pi(\{\hat{\delta}^{el}(r, \gamma_v)\}, \kappa) \quad (55)$$

And for the local Young's modulus:

$$E^{el} = \mathbb{M}(\{\delta\}^{el}, E, E_{min}, \kappa) = \\ = \Pi(\{\hat{\delta}^{el}(r, \gamma_c)\}, \kappa)E \quad (56)$$

Where equation (25) is used to compute $\left\{\hat{\delta}^{el}\right\}$.

Finally, the proposed unified approach can also recover MNA. In fact setting $W_i = m_i w(v_i, h_i, \varepsilon_i)$, $p \to \infty$ and $R = \frac{1}{2}$ and using numerical integration for the integrals in equation (47) with just a single Gauss point one gets:

$$\delta_i^{el} \approx W_i = m_i^{\gamma} w_i^{el} \quad (57)$$

This time for the local densities:

$$\mathbb{V}(\left\{\delta^{el}\right\}, \kappa) = \Pi(\{\delta^{el}\}_v, \kappa) \quad (58)$$

And for the Young modulus:

$$\mathbb{M}(\left\{\delta^{el}\right\}, \kappa) = E_{min} + (E - E_{min})\Pi\left(\{\delta^{el}\}_c, \kappa\right)^{p_b} \quad (59)$$

A summary of the parameters to be used in the proposed Generalized Geometric Projection approach to recover all of the three reviewed methods is provided in table 1.

Note that for the proposed GGP approach, it is not only possible to recover existing strategies, but it is also possible to adapt an existing technique by changing only R and N_{GP}., in order to potentially improve the analysis and optimization behaviour. In this paper we will then refer to: Adapted Moving Morphable Components method (AMMC), Adapted Geometry Projection (AGP) and to Adapted Moving Node Approach (AMNA), when using respectively MMC, GP or MNA parameters in table 1 with the only exceptions of number of Gauss points in each sampling window N_{GP} and of the sampling window size R. In figure 9 the Adapted Moving Node Approach is applied to the same example considered in figure 1a to compute ρ^{el} distribution on a uniform 50×50 mesh and investigates the variation of both R and N_{GP}. In this case we considered MNA characteristic function with a relatively small ε. When just one Gauss point is employed for the numerical integration, R has no effect on the final ρ^{el} distribution. One can observe that increasing N_{GP} smoothens the ρ^{el} variations around the bar ends. On the other hand increasing the value of R smoothens the variation between full and voids elements. These effects are important from the simulation and optimization point of view as will be pointed out in the implementation section.

2.5 Geometric assembly

As discussed in the previous subsections, several approaches were reviewed for making the union or the assembly of geometric primitives. In the first place, we want to point out, as it was done by Norato et al. [35], that the assembly of 2D components can be seen as a merging operation (the component's thickness doesn't change at the intersection) or as an overlapping operation (the component thickness is summed). In the first case one is interested in determining the union of the geometry produced by each component, while in the second case the geometry are simply overlapped in the out of plane direction. Since the stiffness matrix of each finite element is proportional to both the Young's modulus and the out of plane thickness, the local volume fraction of each component could be simply summed up in this case and used to determine an equivalent Young's Modulus that takes into account both the effect of material and out of plane thickness. This ambiguity does not exist in 3D topology optimization where the only possibility to make the assembly is the merging strategy. The rest of this paragraph will then focus on the strategy that can be adopted to merge component's geometries. Firstly one can observe that depending on the considered approach, the assembly is carried out either on local volume fractions or more indirectly through topology description functions (TDF) as in Zhang et al. [71]. [6] In [75] a comprehensive study of application of Boolean operations is reviewed for implicit geometry description (R-functions or TDF). In this context we first want to consider the case when the geometric assembly is applied at the level of the density field. The main advantage of this case consists in being able to treat the local volume fraction coming from each component projection as a pseudo-logical value. In fact let's consider an input vector $\{z\} \in \{0,1\}^n$. In order to make the logic union of all the entry vectors, one can consider either one of the following approaches:

$$\Pi_a(\{z\}) = \min\left(1, \sum_{i=1}^{n} z_i\right) \quad (60)$$

$$\Pi_b(\{z\}) = 1 - \prod_{i=1}^{n}(1 - z_i) \quad (61)$$

$$\Pi_{max}(\{z\}) = \max_i z_i \quad (62)$$

For a logical entry vector $\{z\} \in \{0,1\}^n$, $\Pi_a(\{z\}) = \Pi_b(\{z\}) = \Pi_{max}(\{z\})$. On the other hand when $\{\mathbf{z}\} \in]0,1[^n$ then $\Pi_a(\{z\}) \neq \Pi_b(\{z\}) \neq \Pi_{max}(\{z\})$. The asymptotic density operator $\Pi_a(\{z\})$ first makes an

[6] The characteristic function of the union of sets can be easily computed as the maximum of the characteristic functions of each set. The same can be stated for TDFs.

Table 1: Choice to be made to recover all other approaches using Generalized Geometric Projection

Method	MMC	GP	MNA
W^c	$H_\epsilon(\chi^{el})^q$	$\tilde{\delta}_i^{el} m_i^{\gamma_c}$	$m_i^{\gamma_c} w_i^{el}$
W^v	$H_\epsilon(\chi^{el})$	$\tilde{\delta}_i^{el} m_i^{\gamma_v}$	$m_i^{\gamma_v} w_i^{el}$
p	∞	∞	∞
R	$\frac{\sqrt{3}}{2}dx$	$\frac{1}{2}dx$	$\frac{1}{2}dx$
N_{GP}	4	1	1
$\mathbb{V}$	$\frac{\sum_{j=1}^4 H_\epsilon(\chi_j^{el})}{4}$	$\Pi(\{\hat{\delta}^{el}\}_v, \kappa)$	$\Pi(\{\delta^{el}\}_v, \kappa)$
$\mathbb{M}$	$\frac{\sum_{j=1}^4 (H_\epsilon(\chi_j^{el}))^q}{4}$	$\Pi(\{\hat{\delta}^{el}\}_c, \kappa)E$	$E_{min} + (E - E_{min})\Pi(\{\delta^{el}\}_c, \kappa)^{p_b}$

overlap of the component's density and then saturate the result to 1. This approach was employed in the master thesis of Overvelde [37]. The minimum between 1 and the value of the sum can be realized by a regular saturation function that is detailed later in this paragraph. The boolean operator $\Pi_b(\{z\})$ can be recognized as the one employed by the MMB [19] approach in order to make the union of bar components. For the third approach, since the maximum is an irregular function, in the literature it is often replaced with its regular approximations. In the context of topology optimization we can cite the p-norm and the p-mean [13], the KreisselmeierSteinhauser (KS) functional [23] and the more recent induced approaches [22].Often these approximations are employed in structural optimization with stress constraints in order to reduce the number of constraints in the optimization problem. Here we review these methods and some important properties relative to the maximum operator. Given an input vector $\{\mathbf{z}\} \in \mathbb{R}^n$, and the constant of aggregation $\kappa \in \mathbb{R}^+$, the smooth approximation Π of the maximum operator is defined as: $\Pi : (\mathbb{R}^n, \mathbb{R}^+) \to \mathbb{R} \mid (\{\mathbf{z}\}, \kappa) \to \Pi(\{\mathbf{z}\}, \kappa)$ and

$$\lim_{\kappa \to \infty} \Pi(\{\mathbf{z}\}, \kappa) = \max(\{\mathbf{z}\}) = z_{max} \tag{63}$$

Lets consider the p-norm Π_{pm} and the p-mean Π_{pn} [13]. For these approaches one can make the assumption that an input vector $\{\mathbf{z}\}$ has non negative components, thus:

$$\Pi_{pm}(\{\mathbf{z}\}, \kappa) = \left(\frac{1}{n}\sum_{j=1}^{n} z_j^\kappa\right)^{\frac{1}{\kappa}} \leq z_{max} < \left(\sum_{j=1}^{n} z_j^\kappa\right)^{\frac{1}{\kappa}} = \\ = \Pi_{pn}(\{\mathbf{z}\}, \kappa) \tag{64}$$

One can also have negative inputs but a double correction has to be made in order to have all non-negative inputs when elevating to the power κ. For instance one can chose a positive value z_p so that $z_j + z_p > 0 \ \forall j = 1, 2, ..., n$ with this modification one can compute:

$$\Pi_{pm}^p(\{\mathbf{z}\}, \kappa, z_p) = \left(\frac{1}{n}\sum_{j=1}^{n} (z_j + z_p)^\kappa\right)^{\frac{1}{\kappa}} - z_p \tag{65}$$

$$\Pi_{pn}^p(\{\mathbf{z}\}, \kappa, z_p) = \left(\sum_{j=1}^{n} (z_j + z_p)^\kappa\right)^{\frac{1}{\kappa}} - z_p \tag{66}$$

We will also review here both lower bound KS function Π_{KS}^l and the KS function Π_{KS} [23]:

$$\Pi_{KS}^l(\{\mathbf{z}\}, \kappa) = \frac{1}{\kappa}\log\left(\frac{1}{n}\sum_{j=1}^{n} e^{\kappa z_j}\right) \leq z_{max} < \\ < \frac{1}{\kappa}\log\left(\sum_{j=1}^{n} e^{\kappa z_j}\right) = \Pi_{KS}(\{\mathbf{z}\}, \kappa) \tag{67}$$

Finally we considered also the induced exponential Π_{IE} [22]:

$$\Pi_{IE}(\{\mathbf{z}\}, \kappa) = \frac{\sum_{j=1}^n z_j e^{\kappa z_j}}{\sum_{j=1}^n e^{\kappa z_j}} \leq z_{max} \tag{68}$$

In figure 10, 11, 12 and 13 all reviewed operators are applied to the vector $\{\mathbf{z}\} = \{x, 10xe^{1-10x}, 4x(1-x)\}$ for $x \in [0, 1]$. A first important remark is that p-mean, lower bound KS function and induced exponential operator are always less than or equal to the maximum. The equality being true in the case of uniform value for the entry vector i.e.:

$$\Pi_{pm}(\{\mathbf{z}\}, \kappa) = \Pi_{KS}^l(\{\mathbf{z}\}, \kappa) = \Pi_{IE}(\{\mathbf{z}\}, \kappa) = z_{max} \Leftrightarrow \\ \Leftrightarrow z_1 = z_2 = ... = z_n = z_{max} \tag{69}$$

On the other hand boolean, asymptotic density, p-norm and KS functions are always strictly greater than the maximum function. A second remark is that most reviewed approaches (with the exceptions of the asymptotic density and the boolean operator) produce regular approximations of the maximum function and that by increasing the value of the aggregation constant κ,

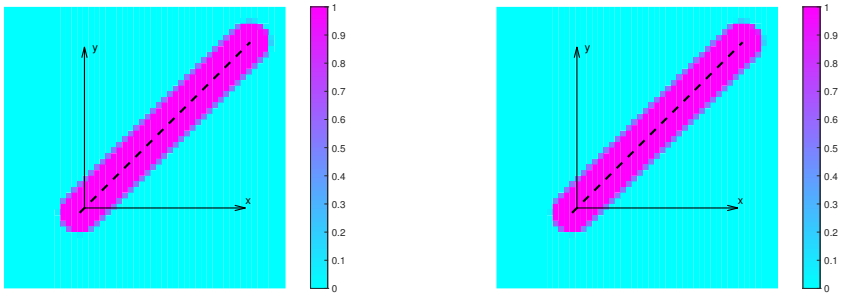

(a) $R = \frac{1}{2}dx$, $N_{GP} = 1$ (b) $R = dx$, $N_{GP} = 1$

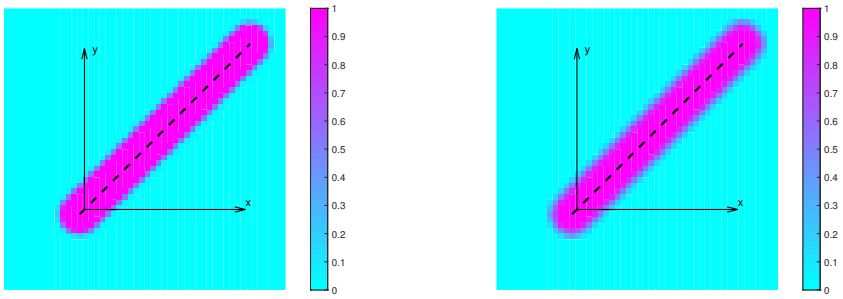

(c) $R = \frac{1}{2}dx$, $N_{GP} = 4$ (d) $R = dx$, $N_{GP} = 4$

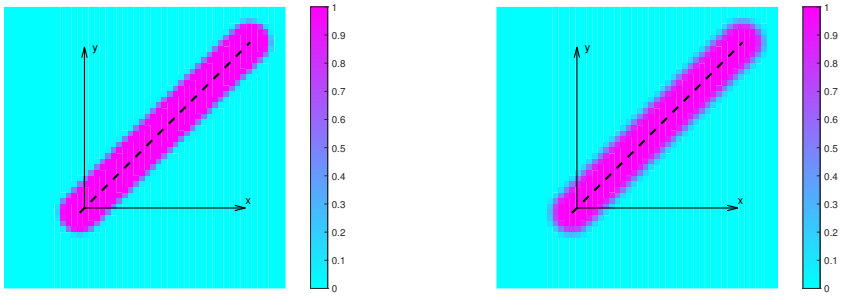

(e) $R = \frac{1}{2}dx$, $N_{GP} = 9$ (f) $R = dx$, $N_{GP} = 9$

Fig. 9: Distribution of ρ^{el} for the generic component of figure 1a and for a 50×50 mesh over the domain of X_g for carying number of Gauss points. We considered MNA characteristic functions $X = 1, Y = 1, L = 3, h = 0.5, \theta = \frac{\pi}{4}, \gamma = 3, \varepsilon = 0.07$ as for MNA. The mesh size dx along the x direction was considered as $dx = 0.07$.

all approaches tend to recover the maximum function as requested in equation (63). At the same time high values of κ reduces the smoothness of the approximated function. A third important remark is that the absolute value of the discrepancy between z_{max} and the approximation are maximized in the following way depending on the aggregation approach employed:

- For p-norm and KS function the worst accuracy corresponds to a uniform entry vector $\mathbf{z}$.
- For p-mean and lower bound KS function the worst accuracy corresponds to a vector $\mathbf{z}$ so that: $z_i = u_b \Leftrightarrow i = i_{max}$ and $z_i = l_b \forall i \neq i_{max}$. Where u_b and l_b are respectively the lower and the upper bound of entry vector components.
- For the induced exponential operator the worst accuracy is reached in intermediate cases

Coming back to the application of these functions to the component assembly, one should consider the following implications:

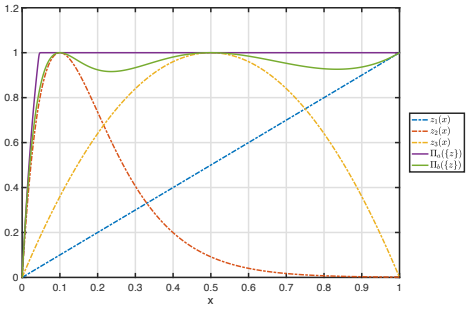

Fig. 10: Application of asymptotic density operator Π_a and of boolean operator Π_b to the vector $\mathbf{z}$ of 3 variables,$z_1(x) = x, z_2(x) = 10xe^{1-10x}, z_3(x) = 4x(1-x)$. The minimum function necessary to carry out the evaluation of Π_a is replaced by the regular approximation of the saturation function of equation (72).

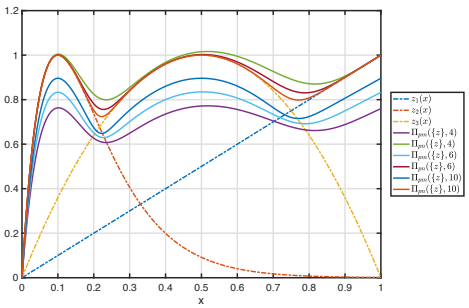

Fig. 11: Application of p-norm Π_{pn} and p-mean Π_{pm} operator for $\kappa = 4, 6, 10$ to the vector $\mathbf{z}$ of 3 variables,$z_1(x) = x, z_2(x) = 10xe^{1-10x}, z_3(x) = 4x(1-x)$.

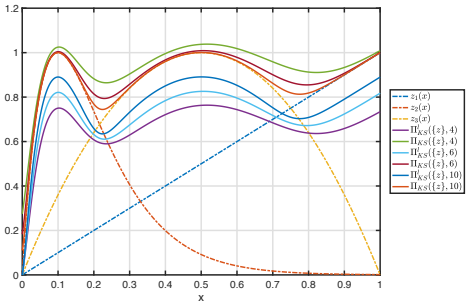

Fig. 12: Application of KS Π_{KS} and lower bound KS Π^l_{KS} function for $\kappa = 4, 6, 10$ to the vector $\mathbf{z}$ of 3 variables, $z_1(x) = x, z_2(x) = 10xe^{1-10x}, z_3(x) = 4x(1-x)$.

- Asymptotic density and Boolean operator are thought to be used on pseudo-logical input, i.e. $\in [0, 1]$. They could also be adopted for TDF but some re-scaling of the input should be adopted to have a meaningful behavior of both operators.
- If the assembly is made on TDFs as in Zhang et al. [71], p-norm and p-mean cannot be employed as they are, but they need to be modified in order to avoid a negative value of the argument of the power.
- When considering TDF applications, one is free to use both KS functions and the induced exponential operator without particular numerical difficulties.
- On the other hand when one wants to apply these functions directly to local volume fractions, some difficulties arise. As the final local density must be lower than 1, the KS function and the p-norm cannot be used since their output can possibly be greater than 1. On the other hand p-mean, lower bound KS function and induced exponential can be used, but in the case of completely non overlapped components the resulting maximal projected density can be inferior to 1. This affects the projected Finite Element Model stiffness and depending on the number of components that describe the solution, can produce inaccurate values of the final compliance. Nevertheless one can control this gap increasing the value of κ. On the other hand as aforementioned this plays a role on the projection smoothness, which can increase or prevent optimization convergence.

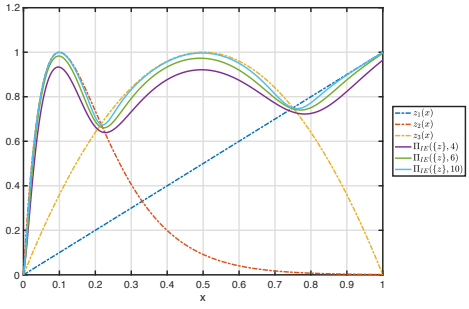

Fig. 13: Application of induced exponential aggregation function Π_{IE} for $\kappa = 4, 6, 10$ to the vector $\mathbf{z}$ of 3 variables,$z_1(x) = x, z_2(x) = 10xe^{1-10x}, z_3(x) = 4x(1-x)$.

To overcome these issues, we propose here to apply a regular approximation of the saturation function to the aggregation operator. This function is defined as:

$$S_t(x) = \min\left(1, \max\left(\frac{x}{\tilde{x}}, 0\right)\right) \tag{70}$$

As it is non regular, we further propose to replace it with the KS approximation:

$$s_b(x, \kappa_s) = -\frac{1}{\kappa_s}\log\left(\exp(-\kappa_s) + \frac{1}{1+\exp\left(\kappa_s \frac{x}{\tilde{x}}\right)}\right) \tag{71}$$

where κ_s is an aggregation constant that can be chosen to be very high ($\kappa_s \geq 100$) in order to get good

approximation of $S_t(x)$. To improve the model accuracy in case of absence of material, a re-scaling of the saturation function is applied i.e.:

$$s_t(x, \kappa_s) = \frac{s_b(x, \kappa_s) - s_b(0, \kappa_s)}{1 - s_b(0, \kappa_s)} \tag{72}$$

This saturation function is represented for several values of the parameter $\tilde{x}$ in figure 14.

Finally the saturated operator will be defined as:

$$P_s(\{z\}, \kappa, \kappa_s) = s_t(\Pi(\{z\}, \kappa), \kappa_s) \tag{73}$$

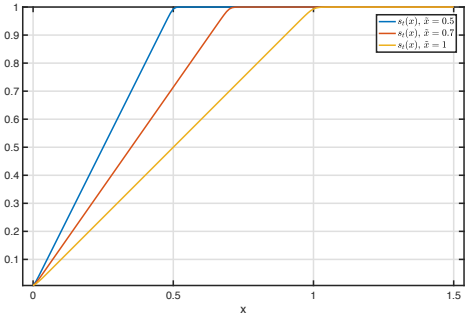

Fig. 14: Proposed saturation function $s_t(x)$ for $\kappa_s = 100$, $\tilde{x} = 0.5$, $\tilde{x} = 0.7$ and $\tilde{x} = 1$.

Note that the value $\tilde{x}$ has to be chosen in order to ensure that, when only one component is projected on the mesh element's centroid, the maximum value of projected local volume fraction is still equal to 1:

$$\tilde{x}_a = \tilde{x}_{KS} = \tilde{x}_{pn} = 1 \tag{74}$$

$$\tilde{x}^l_{KS} = 1 + \frac{1}{\kappa} \log\left(\frac{1 + (n-1)e^{-\kappa}}{n}\right) \tag{75}$$

$$\tilde{x}_{pm} = \left(\frac{(n-1)\, z_p^{\kappa} + (z_p + 1)^{\kappa}}{n}\right)^{\frac{1}{\kappa}} - z_p \tag{76}$$

$$\tilde{x}_{IE} = \frac{1}{1 + (n-1)e^{-\kappa}} \tag{77}$$

The results of the application of the saturation function is applied o the smooth approximation of the maximum operator is illustrated in figures 15,16,17 . One can observe that even when only one component projects to a local volume fraction of 1, the corresponding saturated local volume fraction is nearly at the value of 1 for all reviewed approaches. In order to show the effect of the components assembly and of the saturation, several approaches have been tested on the same configuration and the results presented in figure 18. Another important remark is that without the saturation the p-mean, lower bound KS and induced exponential operator do not achieve the desired final density, i.e. ρ^{el} is

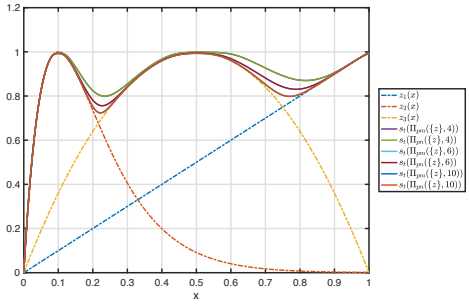

Fig. 15: Application of the proposed saturated p-norm $s_t(\Pi_{pn})$ and p-mean $s_t(\Pi_{pm})$ operator for $\kappa = 4, 6, 10$ to the vector $\mathbf{z}$ of 3 variables,$z_1(x) = x, z_2(x) = 10xe^{1-10x}, z_3(x) = 4x(1-x)$. One can observe the effect of the saturation since, there are no saturated value greater than 1. Moreover for $x = 1$ and $x = 0$, when just one component of the vector $\{z\}$ are equal to 1 and the others are 0, the saturation ensures again a value of 1.

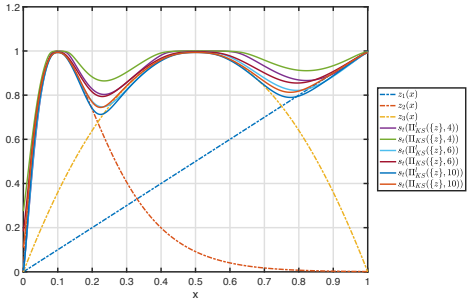

Fig. 16: Application of the proposed saturated KS $s_t(\Pi_{KS})$ and lower bound KS $s_t(\Pi^l_{KS})$ function for $\kappa = 4, 6, 10$ to the vector $\{z\}$ of 3 variables, $z_1(x) = x, z_2(x) = 10xe^{1-10x}, z_3(x) = 4x(1-x)$. One can observe the effect of the saturation since, there are no saturated value greater than 1. Moreover for $x = 1$ and $x = 0$, when just one component of the vector $\{z\}$ are equal to 1 and the others are 0, the saturation ensures again a value of 1.

not 1 when just one of the two components projects to a density of 1. On the other hand this issue is correctly addressed by the saturation procedure proposed here.

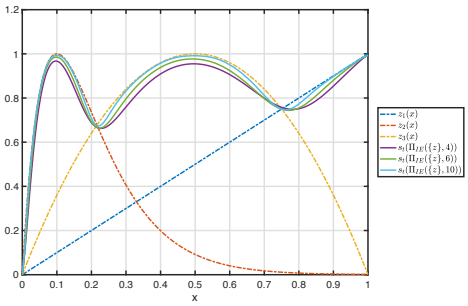

Fig. 17: Application of the proposed saturated induced exponential aggregation function $s_t(\Pi_{IE})$ for $\kappa = 4, 6, 10$ to the vector $\mathbf{z}$ of 3 variables,$z_1(x) = x, z_2(x) = 10xe^{1-10x}, z_3(x) = 4x(1-x)$. One can observe the effect of the saturation since, there are no saturated values greater than 1. Moreover for $x = 1$ and $x = 0$, when just one component of the vector $\{z\}$ are equal to 1 and the others are 0, the saturation ensures again a value of 1.

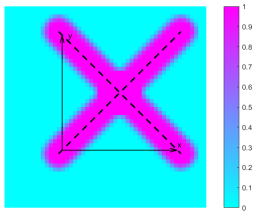

(a) asymptotic

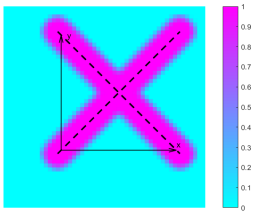

(b) boolean

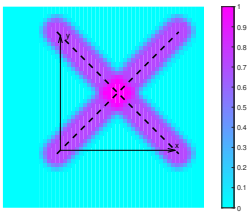

(c) p-mean, $z_p = 1$

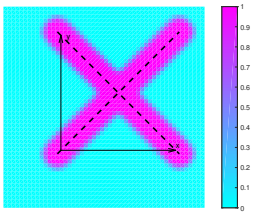

(d) saturated p-mean, $z_p = 1$

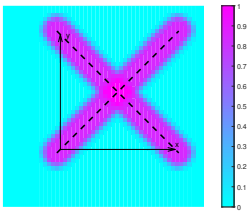

(e) lower bound KS

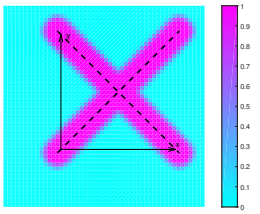

(f) saturated lower bound KS

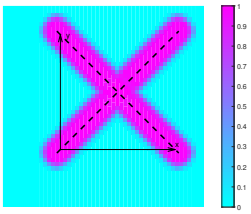

(g) Induced exponential

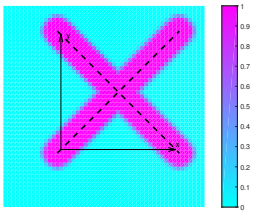

(h) Saturated induced exponential

Fig. 18: Distribution of ρ^{el} for two components for various assembly operators and application or not of saturation. One of the components is in the same configuration of figure 1a, the other with $\theta = -\frac{\pi}{4}$ and for a 50×50 mesh over the domain of X_g. We considered AMNA with $, \gamma = 3, \varepsilon = 0.07, \kappa = 4, \kappa_s = 100$. Where $dx = 0.07$ is the mesh size along the x direction.

2.6 Sensitivity analysis

In this subsection we derive and analyze the gradient of the responses (compliance C and volume fraction V) involved in solving the topology optimization problem considered in equation (13). The aim of this sensitivity analysis is to provide recommendations with respect to good parameter choices in the proposed Generalized Geometric Projection method.

For compliance C and volume fraction V we compute by chain rule:

$$\frac{\partial C}{\partial x_i} = \sum_{el=1}^{N_{el}} \frac{\partial C}{\partial E^{el}} \frac{\partial E^{el}}{\partial x_i} \tag{78}$$

$$\frac{\partial V}{\partial x_i} = \sum_{el=1}^{N_{el}} \frac{\partial V}{\partial \rho^{el}} \frac{\partial \rho^{el}}{\partial x_i} \tag{79}$$

where N_{el} is the number of finite element in the mesh. This can compactly be reformulated as:

$$\left\{\frac{\partial C}{\partial x}\right\} = \left[\frac{\partial E}{\partial x}\right] \left\{\frac{\partial C}{\partial E}\right\} \tag{80}$$

$$\left\{\frac{\partial V}{\partial x}\right\} = \left[\frac{\partial \rho}{\partial x}\right] \left\{\frac{\partial V}{\partial \rho}\right\} \tag{81}$$

In equations (80,81), the right hand side vectors (of size $N_{el} \times 1$) are not different from the one computed for density based topology optimization. On the other hand the matrices $\left[\frac{\partial E}{\partial x}\right]$, $\left[\frac{\partial \rho}{\partial x}\right]$ (of size $N_v \times N_{el}$) are specific to the Generalized Geometry Projection method. Let's derive their analytic expression:

$$\left[\frac{\partial E}{\partial x}\right] = \left[\frac{\partial \mathbb{M}}{\partial x}\right] = \sum_{i=1}^{n} \left[\frac{\partial \delta_i}{\partial x}\right] \left[\frac{\partial \mathbb{M}}{\partial \delta_i}\right] \tag{82}$$

$$\left[\frac{\partial \rho}{\partial x}\right] = \left[\frac{\partial \mathbb{V}}{\partial x}\right] = \sum_{i=1}^{n} \left[\frac{\partial \delta_i}{\partial x}\right] \left[\frac{\partial \mathbb{V}}{\partial \delta_i}\right] \tag{83}$$

where $\left[\frac{\partial \mathbb{M}}{\partial \delta_i}\right]$ and $\left[\frac{\partial \mathbb{V}}{\partial \delta_i}\right]$ are $N_{el} \times N_{el}$ diagonal matrices and the terms $\left[\frac{\partial \delta_i}{\partial x}\right]$ are matrices of size $N_v \times N_{el}$. A first important observation is that $\left[\frac{\partial \delta_i}{\partial x}\right]$ is sparse and only the lines of variables belonging to the i^{th} component will be different from zero i.e. $\left[\frac{\partial \delta_i}{\partial x_i}\right]$ $(6 \times N_{el})$. This means that each row of $\left[\frac{\partial E}{\partial x}\right]$, $\left[\frac{\partial \rho}{\partial x}\right]$ will have just one contribution coming from the component defined by the corresponding variable. Let's first derive the terms in the diagonal of $\left[\frac{\partial \mathbb{M}}{\partial \delta_i}\right]$ and $\left[\frac{\partial \mathbb{V}}{\partial \delta_i}\right]$. As an example here we considered MNA characteristic functions and the saturation function applied after the geometry assembly:

$$\frac{\partial \mathbb{M}^{el}}{\partial \delta_i^{el}} = \frac{\partial \mathbb{M}^{el}}{\partial P_s} \frac{\partial P_s}{\partial \Pi} \frac{\partial \Pi}{\partial \delta_i^{el}} \tag{84}$$

$$\frac{\partial \mathbb{V}^{el}}{\partial \delta_i^{el}} = \frac{\partial \mathbb{V}^{el}}{\partial P_s} \frac{\partial P_s}{\partial \Pi} \frac{\partial \Pi}{\partial \delta_i^{el}} \tag{85}$$

The evaluation of $\frac{\partial \mathbb{M}^{el}}{\partial s_t}$ and of $\frac{\partial \mathbb{V}^{el}}{\partial s_t}$ depends on the choice made among the existing functions. For AMNA one gets:

$$\frac{\partial \mathbb{M}^{el}}{\partial P_s} = p_b (E - E_{min}) s_t^{pb-1} \tag{86}$$

$$\frac{\partial \mathbb{V}^{el}}{\partial P_s} = 1 \tag{87}$$

For the saturation function one can get:

$$\frac{\partial P_s}{\partial \Pi} = \frac{\exp\left(\kappa_s \frac{\Pi}{\tilde{\Pi}}\right) \left(\exp\left(\kappa_s \frac{\Pi}{\tilde{\Pi}}\right) + 1\right)^{-2}}{\tilde{\Pi} \left(\exp\left(-\kappa_s\right) + \frac{1}{\exp\left(\kappa_s \frac{\Pi}{\tilde{\Pi}}\right)+1}\right)} \frac{1}{1 - s_b(0, \kappa_s)} \tag{88}$$

Where $\tilde{\Pi}$ has to be computed according to equations (74-77). For the computation of $\frac{\partial \Pi}{\partial \delta_i^{el}}$ the interested reader can find the computation for KS_l, KS and induced exponential in [22]. For p-norm and p-mean we detail their computations as follows:

$$\frac{\partial \Pi^p_{pm}}{\partial \delta_i^{el}} = \frac{1}{n} \left(\delta_i^{el} + z_p\right)^{\kappa - 1} \left(\frac{1}{n} \sum_{j=1}^{n} \left(\delta_j^{el} + z_p\right)^{\kappa}\right)^{\frac{1}{\kappa} - 1} \tag{89}$$

$$\frac{\partial \Pi^p_{pn}}{\partial \delta_i^{el}} = \left(\delta_i^{el} + z_p\right)^{\kappa - 1} \left(\sum_{j=1}^{n} \left(\delta_j^{el} + z_p\right)^{\kappa}\right)^{\frac{1}{\kappa} - 1} \tag{90}$$

For the term $\left[\frac{\partial \delta_i}{\partial x_i}\right]$ when using Gauss quadrature one has:

$$\left[\frac{\partial \delta_i}{\partial x_i}\right] = \frac{\sum_{k=1}^{N_{GP}} \psi_k \left[\frac{\partial W_{ik}}{\partial x_i}\right]}{\sum_{k=1}^{N_{GP}} \psi_k} \tag{91}$$

Finally for the derivatives of $\left[\frac{\partial W_{ik}}{\partial x_i}\right]$ one can again use the chain rule and the hypothesis of MNA characteristic functions. For each row of $\left[\frac{\partial W_{ik}}{\partial x_i}\right]$ one has a different expression depending on which variable is being considered. Note that from now on, index and parenthesis notations are neglected for brevity. We can then derive the analytic expression of each derivatives, knowing that each expression has to be applied to each

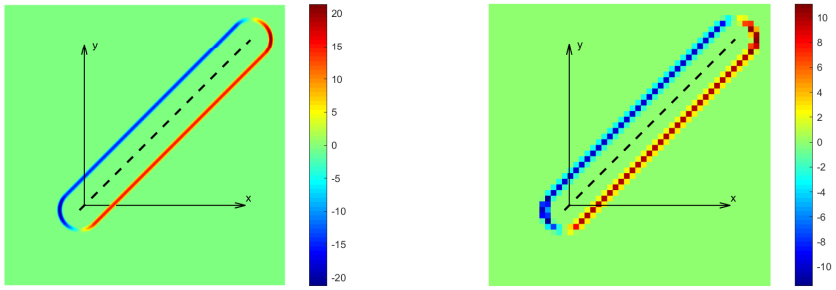

(a) $\frac{\partial W}{\partial X}$ (b) $\frac{\partial \delta}{\partial X}$,$R = \frac{1}{2}dx$, $N_{gp} = 4$

(c) $\frac{\partial \delta}{\partial X}$,$R = \frac{1}{2}dx$, $N_{gp} = 9$ (d) $\frac{\partial \delta}{\partial X}$,$R = dx$, $N_{gp} = 4$

Fig. 19: Derivatives distribution of W and δ with respect to X for varying number of Gauss Points N_{GP} in the sampling window and varying sampling window size R. We considered Adapted Moving Node Approach with the generic component of figure 1a in the configuration $X = 1, Y = 1, L = 3, h = 0.5, \theta = \frac{\pi}{4}, \gamma = 3, \varepsilon = 0.07$ and $dx = 0.07$ for a 50×50 mesh over the domain of X_g.

couple of components and point of Gauss of each sampling window. For m variables one has in fact:

$$\frac{\partial W}{\partial m} = \gamma m^{\gamma-1} w \tag{92}$$

For variable h using the chain rule:

$$\frac{\partial W}{\partial h} = m^{\gamma} \left\{ \frac{\partial w}{\partial h} \right\} \tag{93}$$

where

$$\frac{\partial w}{\partial h} = \begin{cases} \frac{\partial a_2}{\partial h} \upsilon^2 + \frac{\partial a_1}{\partial h} \upsilon + \frac{\partial a_0}{\partial h} & \text{if } l < \upsilon < u \ , \\ 0 \quad \text{otherwise.} \end{cases} \tag{94}$$

and where

$$\frac{\partial a_2}{\partial h} = -\frac{3}{\varepsilon^3} \tag{95}$$

$$\frac{\partial a_1}{\partial h} = 6\frac{h}{\varepsilon^3} \tag{96}$$

$$\frac{\partial a_0}{\partial h} = 3\frac{\varepsilon^2 - h^2}{4\varepsilon^3} \tag{97}$$

For the other components, following derivatives are obtained by the chain rule:

$$\frac{\partial W}{\partial X} = m^{\gamma} \frac{\partial w}{\partial \upsilon} \left(\frac{\partial \upsilon}{\partial \varrho} \frac{\partial \varrho}{\partial X} + \frac{\partial \upsilon}{\partial \phi} \frac{\partial \phi}{\partial X} \right) \tag{98}$$

$$\frac{\partial W}{\partial Y} = m_i^{\gamma} \frac{\partial w}{\partial \upsilon} \left(\frac{\partial \upsilon}{\partial \varrho} \frac{\partial \varrho}{\partial Y} + \frac{\partial \upsilon}{\partial \phi} \frac{\partial \phi}{\partial Y} \right) \tag{99}$$

$$\frac{\partial W}{\partial L} = m_i^{\gamma} \frac{\partial w}{\partial \upsilon} \frac{\partial \upsilon}{\partial L} \tag{100}$$

$$\frac{\partial W}{\partial \theta} = m_i^{\gamma} \frac{\partial w}{\partial \upsilon} \frac{\partial \upsilon}{\partial \phi} \frac{\partial \phi}{\partial \theta} \tag{101}$$

That can be evaluated by the use of:

$$\frac{\partial w}{\partial \upsilon} = \begin{cases} 3a_3\upsilon^2 + 2a_2\upsilon + a_1 & \text{if } l < \upsilon < u \ , \\ 0 \quad \text{otherwise.} \end{cases} \tag{102}$$

$$\frac{\partial \upsilon}{\partial \varrho} = \begin{cases} \frac{2\,\varrho - L\,|\cos(\phi)|}{2\,\upsilon} & \text{if } \frac{L^2}{4} < \varrho^2 \cos(\phi)^2 \\ |\sin(\phi)| & \text{if } \frac{L^2}{4} \geq \varrho^2 \cos(\phi)^2 \end{cases} \tag{103}$$

$$\frac{\partial \upsilon}{\partial \phi} = \begin{cases} \frac{L\,\varrho\,\mathrm{sign}(\cos(\phi))\,\sin(\phi)}{2\,\upsilon} & \text{if } \frac{L^2}{4} < \varrho^2 \cos(\phi)^2 \\ \varrho\,\mathrm{sign}(\sin(\phi))\,\cos(\phi) & \text{if } \frac{L^2}{4} \geq \varrho^2 \cos(\phi)^2 \end{cases}$$

(104)

$$\frac{\partial v}{\partial L} = \begin{cases} \frac{\frac{L}{2} - \varrho\,|\cos(\phi)|}{2\,v} & \text{if } \frac{L^2}{4} < \varrho^2 \cos(\phi)^2 \\ 0 & \text{if } \frac{L^2}{4} \geq \varrho^2 \cos(\phi)^2 \end{cases} \tag{105}$$

$$\frac{\partial \varrho}{\partial X} = \frac{X - x}{\varrho} \tag{106}$$

$$\frac{\partial \varrho}{\partial Y} = \frac{Y - y}{\varrho} \tag{107}$$

$$\frac{\partial \phi}{\partial X} = \frac{y - Y}{\varrho^2} \tag{108}$$

$$\frac{\partial \phi}{\partial Y} = \frac{X - x}{\varrho^2} \tag{109}$$

$$\frac{\partial \phi}{\partial \theta} = -1 \tag{110}$$

Let us note that based on these definitions some sensitivities could be either not defined or not continuous. However note that by respecting the condition $h > \varepsilon$ these issues are avoided. In figures 19,27,28,29 and 30 the Generalized Geometry Projection is employed to study the distribution of gradients of both W and δ. The effect of both sampling window size and number of Gauss points is investigated. We can then make some observations and recommendations:

- All represented gradient components even if defined piece-wisely are regular.
- All gradient components of W take values different from zero only in the component's transition zone.
- After applying the Generalized Geometry Projection gradient components of δ are averaged on the sampling windows and as a consequence are much smaller. Increasing the number of Gauss points, derivatives of δ become smoother, which is benefic for the optimization. Increasing the sampling window size increases the thickness of the transition zone as well as the gradients of δ, which also has benefic effects as will be further illustrated in the next section.

3 Numerical investigations

In this section we investigate, on several numerical applications, the effects of the various parameters (such as number of Gauss points N_{GP} and sampling windows size R) present in the Generalized Geometry Projection, in terms of finite element analysis accuracy and topology optimization problem ill conditioning. In the first subsection we consider a simple cantilever beam that can be modelled using both the Geometry projection scheme and classic Euler beam finite element. The aims of this analysis is to investigate the model accuracy and limits when using Generalized Geometry Projection. In the topology optimization subsection we investigate the behaviour of Generalized Geometry Projection to be used for the resolution of a 2D topology optimization problem: the short cantilever beam. This problem has been widely studied by several works, here it is considered only to assess a common problem that every approach is faced with and for which we provide practical recommendations.

3.1 Parametric study of a cantilever beam

We first consider a simple test case that can also be compared to Theoretical results: the cantilever beam (c.f. figure 20). In table 2 the numerical values chosen for our numerical experiment are detailed. Here we will

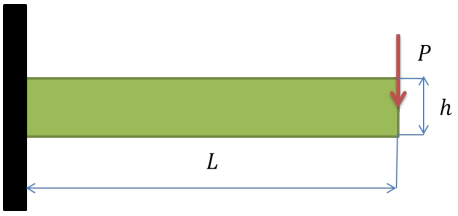

Fig. 20: Representation of the considered cantilever beam problem.

investigate the effect of thickness h, of the number of Gauss points N_{GP} and of the sampling window size (of the Generalized Geometry Projection) R as well as the effect of the topology optimization method employed (AMMC, AGP or AMNA) on the total compliance C and volume fraction V (defined with respect to the total volume occupied by the solid finite element mesh). Using the well known Euler beam model, one can in fact compute analytically the compliance and the volume fraction of the beam:

$$C = \frac{4PL^3}{Ebh^3} = \frac{4 \times 10^6}{h^3} \tag{111}$$

$$V = \frac{bLh}{n_{elx} n_{ely}} = \frac{h}{50} \tag{112}$$

The reader can observe that for the range of values selected for $h \in [1, 10]$ the ratio between the beam lenght L and its cross section area $A = bh$ is $\frac{L}{A} \in [10, 100]$, large enough to consider the hypothesis of Euler beam model reasonable. For this cantilever beam problem we now consider the Generalized Geometry Projection, over the mesh illustrated in figure 21b. The results of this trade study, which varied parameters h , N_{GP}, R and the chosen method, are shown in figures 22,31,32 and 33 and we can make following observations:

Table 2: Parameters retained for the parametric study of the cantilever beam

Parameter name	symbol	value
Material Young Modulus	E	1
Beam Length	L	100
Beam width (out of plane direction)	b	1
Beam height	h	$\in [1, 10]$
Load amplitude	P	1
Number of element in x direction	n_{elx}	100
Number of element in y direction	n_{ely}	50
Poisson ratio	υ	0.3
element size in x direction	dx	1
element size in y direction	dy	1
AMMC parameter α	α	1
AMMC parameter β	β	10^{-3}
AMMC parameter ϵ	ϵ	0.7
AMMC parameter q	q	3
AMMC parameter α	α	1
AGP parameter r	r	1.5
AGP/AMNA parameter γ_v	γ_v	1
AGP/AMNA parameter γ_c	γ_c	1.5
AGP parameter δ_{min}	δ_{min}	10^{-6}
AMNA parameter ε	ε	3
AMNA parameter p_b	p_b	1
AMNA parameter E_{min}	E_{min}	10^{-6}
Aggregation constant for saturation	κ_s	10^2

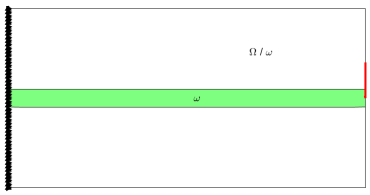

(a) Component plot for the cantilever beam

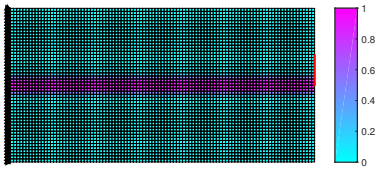

(b) Corresponding density plot distribution ρ^{el}

Fig. 21: Illustration of the Adapted Moving Node Approach (AMNA) for the cantilever beam. A single round ended component ω is considered in the configuration $\{x\} = \{50, 25, 100, 5, 0\}$. The 100×50 2D planar stress solid element mesh covers the domain $\Omega \cong [0, 100] \times [0, 50]$. We set $N_{GP} = 1$ and $R = \frac{1}{2}dx$. The saturation function was employed. The other hyperparameters are summarized in table 2. The round ends of the components fall outsideΩ and are not represented in these figures.

– For all methods one gets better accuracy for higher thicknesses, especially for the compliance C. These effects are closely related to a very well known issue of solid elements with complete integration: the shear-locking effect. The stiffness of thin structures are overestimated when using few element in the thickness direction. As a consequence the mesh size can control the minimal dimension of the components that one can consider in topology optimization without loosing model accuracy.
– For all reviewed adapted methods, mesh induced inflection points in both compliance and volume fraction graph may be observed (i.e. waviness in the respective curves). This is especially the case for small values of h and of N_{GP} and for AMMC.
– Increasing the sampling window size R (for $N_{GP} > 1$) reduces the model compliance.
– Increasing the number of Gauss points N_{GP}, mesh induced phenomena are attenuated for all approaches.

The model behavior is dictated by the transition region at the border of the components, especially for small h, which also explains why AMMC amplifies the mesh induced phenomena. In fact, the transition region thickness being proportional to h, for small value of h and N_{GP}, the transition region is small enough to be located between Gauss point locations. In this situation for small changes of the thickness h both C and V will not change, as can be seen in figure 31. These observation are of course relative to our particular choice of settings for each approach and are not necessarily generalizable to other geometric configuration. Nevertheless, based on the causes mentioned for these effects, they are likely to reoccur in many other situations. As shown, a good choice of the topology optimization parameters h , N_{GP}, R and formulation can however reduce these negative effects. Finally we want to point out the fact that these conclusions are consistent with the observation made in the work of Zhou et al. [78] for geometric feature based topology optimization using level set topology optimization.

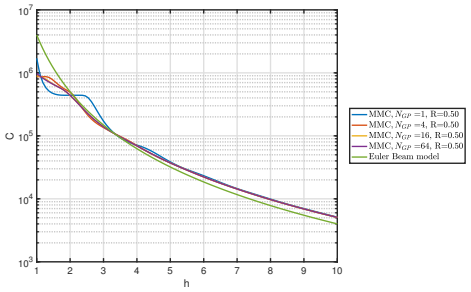

(a) $h - C$ plot for $R = 0.5$, $N_{GP} = \{1, 4, 16, 64\}$

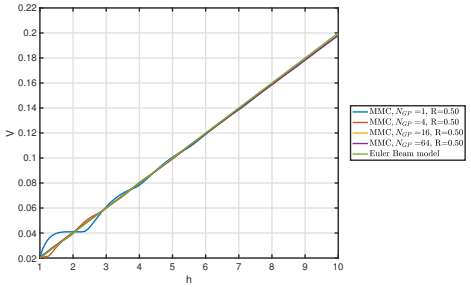

(b) $h - V$ plot for $R = 0.5$, $N_{GP} = \{1, 4, 16, 64\}$

Fig. 22: Cantilever beam parametric study using the AMMC approach for $R = 0.5$. Effect of the sampling window number of Gauss points N_{GP} on the structural compliance and the volume fraction. In each graph we reported in green the true theoretical values based on the analytic beam model. The remainder of results can be found in annexes.

3.2 Topology Optimization of the short cantilever beam

In this subsection we consider the topology optimization of a short cantilever beam, starting from an initial components configuration shown in figure 23. We will investigate on this test case the effects of the number of Gauss points in each sampling window N_{GP} on the optimization convergence, when using the adapted methods based on the proposed GGP framework: AMMC, AGP and AMNA. We employed the well know Method of Moving Asymptotes [44], in the Matlab version distributed by the author [46]. A special rescaling was also adopted to avoid MMA numerical intabilities as explained in appendix 6.3. A saturated KSl aggregation operator was employed to make the geometric union of component for all adapted methods. The design variables are initiated according to figure 23. The stopping criteria employed was on the infinite norm of the configuration variation. The numerical values chosen for all the parameters of both projection and optimization solver are detailed in table 3. In figure 24,25 and 26

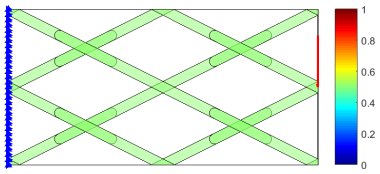

Fig. 23: Initial configuration for the short cantilever topology optimization problem. Components are colored according to the value of m. Blue triangles represents clamped degrees of freedoms. The red arrow represents the applied load. 18 round ended bars are considered for the optimization, i.e. $6 \times 18 = 108$ design variables for both AGP and AMNA and $5 \times 18 = 90$ design variables for AMMC.

the results of the topology optimization problem of a short cantilever beam are considered for several value of N_{GP}.

It is well known that topology optimization problems are multi-modal, i.e. there are many local minima in the problem. Accordingly one can have convergence to several, sometimes different local optima, depending here on both method employed for projection and on the number of Gauss points. In all cases we observe a converge to a reasonable local minimum that is consistent with boundary conditions and load application. We can also observe that as a general tendency, by increasing the number of Gauss points one reduces the iterations at convergence and/ or improves the final compliance of the solution. One should keep in mind that the material update law is different for each approach and this may explain why the same geometric configuration can have different values of compliance and volume fraction for each approach. These results confirm the observations already made for the cantilever parametric study. Considering small values of the transition width and small values for N_{GP}, the optimization solver needs more iterations to converge. Intuitively one can say that this is also a consequence of compliance and volume fraction behaviors that is in these cases perturbed by mesh induced effects.

4 Discussion

The previous results allowed us to investigate the effect of various parameters of the Generalized Geometry Projection (GGP) approach on both simulation and opti-

Table 3: Parameters used for the parametric study of the short cantilever beam

Parameter name	symbol	value
Material Young Modulus	E	1
Design zone width (out of plane direction)	b	1
Load amplitude	P	1
Number of element in x direction	n_{elx}	60
Number of element in y direction	n_{ely}	30
Poisson ratio	υ	0.3
element size in x direction	dx	1
element size in y direction	dy	1
AMMC parameter α	α	1
AMMC parameter β	β	10^{-3}
AMMC parameter ϵ	ϵ	0.866
AMMC parameter q	q	2
AMMC parameter α	α	1
AGP parameter r	r	0.5
AGP/AMNA parameter γ_v	γ_v	1
AGP/AMNA parameter γ_c	γ_c	3
AGP parameter δ_{min}	δ_{min}	10^{-6}
AMNA parameter ε	ε	1
AMNA parameter p_b	p_b	3
AMNA parameter E_{min}	E_{min}	10^{-6}
Aggregation constant for saturation	κ_s	10^2
Aggregation constant	κ	10
MMA moving limit		0.1
MMA initial moving limit		0.01
MMA incremental factor asyincr		1.2
MMA decremental factor asydecr		0.4
MMA parameter albefa		0.1
MMA parameter move		0.5
Stopping criteria, design variable variation		0.001
Minimal x position	x_{min}	-1
Minimal y position	y_{min}	-1
Minimal length	L_{min}	0
Minimal height	h_{min}	1
Minimal angle	θ_{min}	-2π
Minimal component density	m_{min}	0
Maximal x position	x_{max}	$n_{elx}+1$
Maximal y position	y_{max}	$n_{ely}+1$
Maximal length	L_{max}	$\sqrt{n_{elx}^2+n_{ely}^2}$
Maximal height	h_{max}	$\sqrt{n_{elx}^2+n_{ely}^2}$
Maximal angle	θ_{max}	2π
Maximal component density	m_{max}	1

mization. One of the main points these results highlight is that, depending on the geometric characteristic functions employed (transition region width), and on the number of Gauss points in the sampling window, several mesh induced phenomena can detrimentally impact the model responses. One can use several strategies that aim at reducing these phenomena:

– **Increase the component transition region width** to a size large enough to ensure that at least one Gauss point falls inside it. This strategy is possible for all reviewed approaches, is quite simple, and does not represent any significant numerical expense in terms of neither simulation nor optimization. The main drawback of this strategy is that one needs to consider bigger components for a given mesh size. In fact considering component with a thickness h smaller than the transition width, does not ensure sensitivity regularity (For AGP and AMNA). For AMMC the transition width is directly proportional to the component size so that for too small values of h there is not a value of ϵ and α that can be chosen to give sufficiently high values of the transition width.
– **Refine the mesh** keeping the same value of the transition thickness and of the minimal component size. This is an alternative to the previous recommendation which can be seen as strictly equivalent. In this way, obviously one increases the chance of

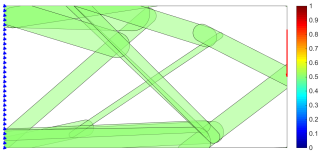

(a) Component plot $N_{GP} = 1$, $R = \frac{1}{2}$

(b) Density plot $N_{GP} = 1$, $R = \frac{1}{2}$

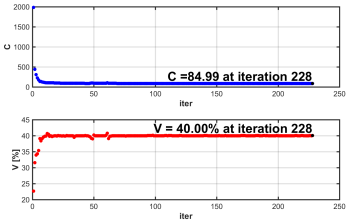

(c) Convergence plot $N_{GP} = 1$, $R = \frac{1}{2}$

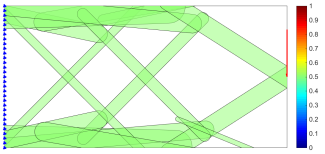

(d) Component plot $N_{GP} = 4$, $R = \frac{1}{2}$

(e) Density plot $N_{GP} = 4$, $R = \frac{1}{2}$

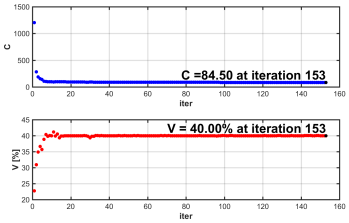

(f) Convergence plot $N_{GP} = 4$, $R = \frac{1}{2}$

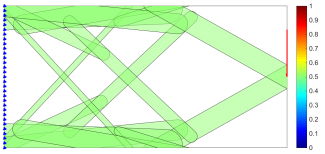

(g) Component plot $N_{GP} = 16$, $R = \frac{1}{2}$

(h) Density plot $N_{GP} = 16$, $R = \frac{1}{2}$

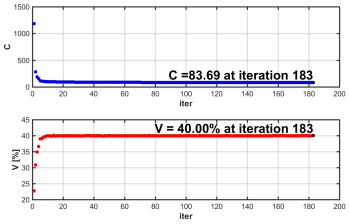

(i) Convergence plot $N_{GP} = 16$, $R = \frac{1}{2}$

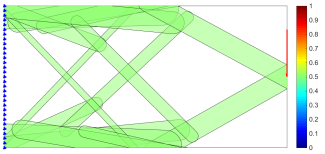

(j) Component plot $N_{GP} = 64$, $R = \frac{1}{2}$

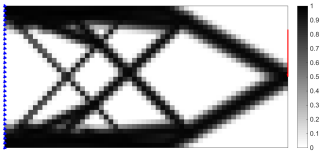

(k) Density plot $N_{GP} = 64$, $R = \frac{1}{2}$

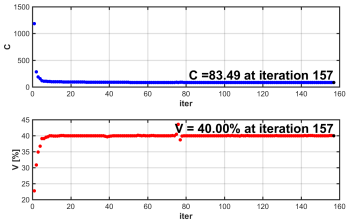

(l) Convergence plot $N_{GP} = 64$, $R = \frac{1}{2}$

Fig. 24: Short Cantilever Beam Topology optimization using the AMMC method for variable number of Gauss points N_{GP}.

having a sampling window Gauss point inside transition region, but this comes at a higher computational cost in terms of both memory and CPU time.

– **Use a multi-resolution approach** [28]. These approaches have also the virtue of filling the transition region with Gauss points. This time the difference with GGP is that the assembly of the stiffness matrix is realized using the contribution given by the point inside each element. This means that from a computational burden point of view this method shares the same cost for the simulation of the original problem but still require more memory than GGP. In fact, in order to build the stiffness matrix one needs in 2D 64 terms coming from each Gauss point to be computed vs the unique value in GGP needed for the assembly. Still as for our approach the shear-locking problem can have an impact on the response coming from an ill refined solution.
– **Use Generalized Geometry Projection** increasing N_{GP}. That is a very inexpensive way to attenu-

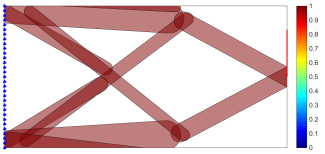

(a) Component plot $N_{GP} = 1$, $R = \frac{1}{2}$

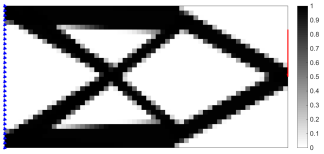

(b) Density plot $N_{GP} = 1$, $R = \frac{1}{2}$

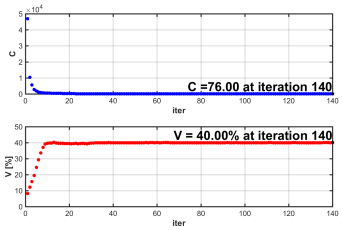

(c) Convergence plot $N_{GP} = 1$, $R = \frac{1}{2}$

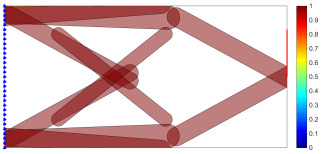

(d) Component plot $N_{GP} = 4$, $R = \frac{1}{2}$

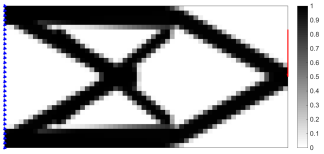

(e) Density plot $N_{GP} = 4$, $R = \frac{1}{2}$

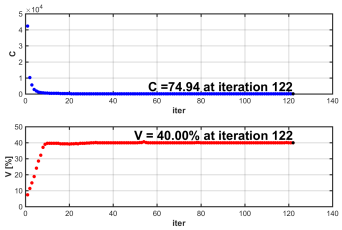

(f) Convergence plot $N_{GP} = 4$, $R = \frac{1}{2}$

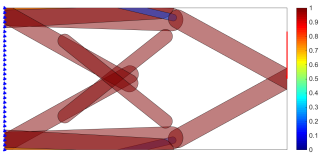

(g) Component plot $N_{GP} = 16$, $R = \frac{1}{2}$

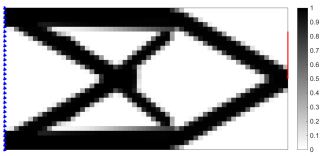

(h) Density plot $N_{GP} = 16$, $R = \frac{1}{2}$

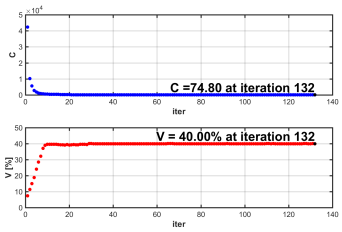

(i) Convergence plot $N_{GP} = 16$, $R = \frac{1}{2}$

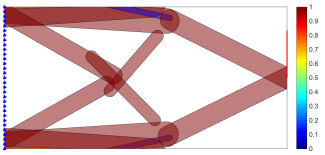

(j) Component plot $N_{GP} = 64$, $R = \frac{1}{2}$

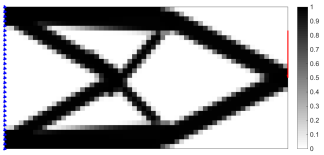

(k) Density plot $N_{GP} = 64$, $R = \frac{1}{2}$

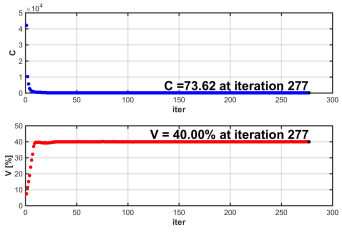

(l) Convergence plot $N_{GP} = 64$, $R = \frac{1}{2}$

Fig. 25: Short Cantilever Beam Topology optimization using the AGP method for variable number of Gauss points N_{GP}.

ate mesh induced inflection points for the responses. In this way one can also consider thinner components in the optimization, with a very small supplementary memory and computational burden coming from the projection. It must be noted that using a clever choice of R and of N_{GP} the computational burden of adapted techniques may be controlled. In fact as is the case in the MMC approach with $N_{GP} = 4$, $R = \frac{\sqrt{3}}{2}dx$,since the sampling window Gauss points coincide with the finite element mesh nodes, one has to compute only $(n_{elx}+1)(n_{ely}+1)$ local volume fractions, instead of $4n_{elx}n_{ely}$ required in the case of non coincidence with other element sampling window Gauss points.

– **Change the computation of sensitivity**. In level set topology optimization approaches the issue of computing design sensitivities is widely studied. Some interesting techniques can also be adapted for the GGP approach, like the boundary integral approach [8] or the narrow-band domain integral scheme [78].

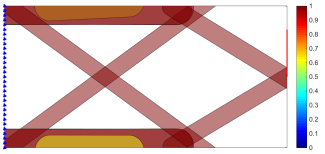

(a) Component plot $N_{GP} = 1$, $R = \frac{1}{2}$

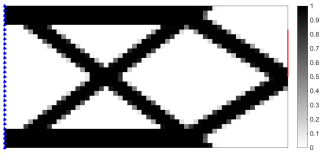

(b) Density plot $N_{GP} = 1$, $R = \frac{1}{2}$

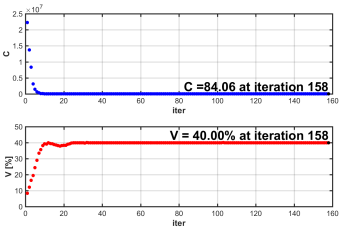

(c) Convergence plot $N_{GP} = 1$, $R = \frac{1}{2}$

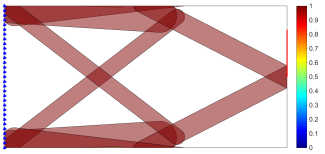

(d) Component plot $N_{GP} = 4$, $R = \frac{1}{2}$

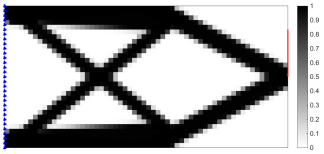

(e) Density plot $N_{GP} = 4$, $R = \frac{1}{2}$

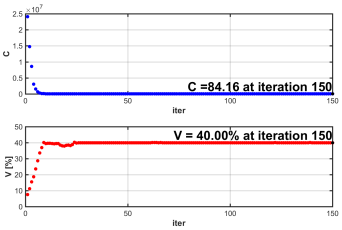

(f) Convergence plot $N_{GP} = 4$, $R = \frac{1}{2}$

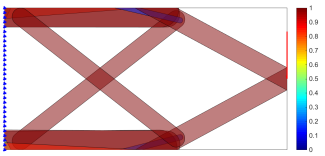

(g) Component plot $N_{GP} = 16$, $R = \frac{1}{2}$

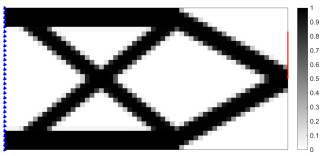

(h) Density plot $N_{GP} = 16$, $R = \frac{1}{2}$

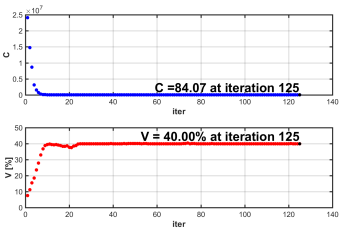

(i) Convergence plot $N_{GP} = 16$, $R = \frac{1}{2}$

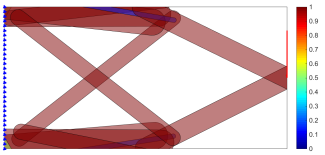

(j) Component plot $N_{GP} = 64$, $R = \frac{1}{2}$

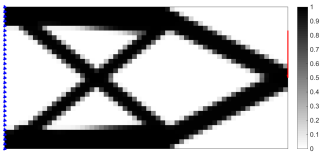

(k) Density plot $N_{GP} = 64$, $R = \frac{1}{2}$

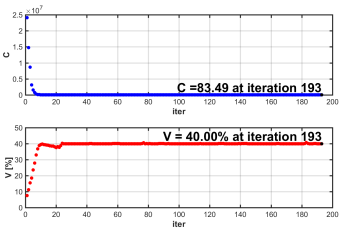

(l) Convergence plot $N_{GP} = 64$, $R = \frac{1}{2}$

Fig. 26: Short Cantilever Beam Topology optimization using the AMNA method for variable number of Gauss points N_{GP}.

– **Use finite differences for characteristic function gradients evaluation** and increase the perturbation step. It must be noted that in this work all Adapted approaches have been implemented using explicit evaluation of characteristic function. It is also possible to deal with saddle points employing finite differences for the gradient of characteristic function, as it is done in MMC [71]. When doing so, the optimization solver could be able to escape from saddle points. This solution comes with an increased computational burden induced by the evaluation of the characteristic function sensitivity in the gauss points. Moreover, the choice of the finite difference represents a non trivial trade off between the avoidance of optimization solver convergence to saddle points and the gradient evaluation accuracy.

5 Conclusions

In this paper, a review of existing approaches for explicit topology optimization, also known as geometric feature based topology optimization was carried out. After a review of recent developments we focused on the method of moving morphable components (MMC), the method of geometric projection (GP) and the moving node approach (MNA), for a common round ended bar geometric primitive. We the proposed the so called Generalized Geometry Projection, as a generalized procedure, encompassing all three approaches (MMC, GP and MNA) as particular cases. We reviewed also different strategies for taking the union of components using smooth approximations of the maximum function. We also introduced a saturation operation whose efficiency was shown on all the reviewed approach in order to avoid detrimental final local volume fractions greater than one. Moreover this procedure ensures a maximal Young's modulus when projecting only one component a time. This avoids a classic problem of the choice of the aggregation constant as a compromise between the simulation accuracy, and the response non-linearity. Based on a sensitivity analysis we showed that the transition region of a component, where the component characteristic function takes intermediate values, is also the only region where its gradients take values different from zero. As a consequence the number of Gauss points in this region can induce discretization effects that were shown to potentially have detrimental consequences in both optimization and simulation. These effects were also numerically investigated on two test cases and recommendations were formulated to avoid them. As future work, we will seek to extend this framework for solving 3D topology optimization problems, including different formulations involving stress based constraints and performance constraints. Another future work direction is to extend this work to several geometric primitives in both 2D and 3D, and to intersections with void components. The analyses and observations made on the studied benchmark problem also motivate the further study of components with a thickness that is comparable with the mesh size. Indeed, in this case all reviewed approach show bad stiffness model accuracy due to the shear-locking effect. With a particular choice of the parameters in the characteristic function for a given choice of parameters for GGP, one could achieve an improved accuracy for a large panel of test cases, including the one where the shear-locking dominate stiffness model. The authors are commited to provide supplementary material for the replication of results in this paper at https://github.com/topggp/GGP-Matlab.

6 Appendices

6.1 Appendix 1: Characteristic function and local volume fraction sensitivity distribution

In this subsection we present the distribution of both characteristic function and local volume fraction sensitivity to the design variables in the example introduced in subsection 2.6. The effect of both the sampling window size and the number of Gauss point is analyzed to compute δ from the same W. An important observation is that by increasing N_{GP} one increases the ability of GGP to adequately capture the narrow distribution of characteristic function sensitivity.

6.2 Appendix 2: Parametric study results on the cantilever beam case

In this section the full plot results from the parametric study on the cantilever beam presented in subsection 3.1 are provided.

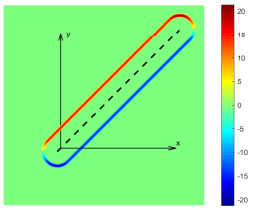

(a) $\frac{\partial W}{\partial Y}$

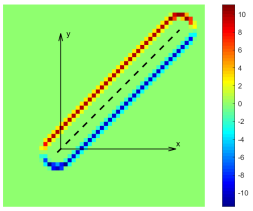

(b) $\frac{\partial \delta}{\partial Y}$,$R = \frac{1}{2}dx$, $N_{gp} = 4$

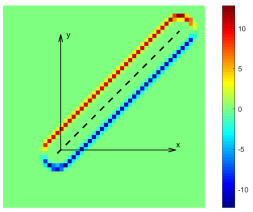

(c) $\frac{\partial \delta}{\partial Y}$,$R = \frac{1}{2}dx$, $N_{gp} = 9$

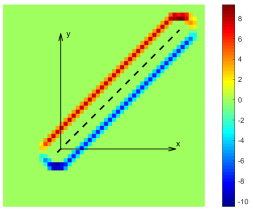

(d) $\frac{\partial \delta}{\partial Y}$,$R = dx$, $N_{gp} = 4$

Fig. 27: Sensitivity distribution of W and δ with respect to Y for varying number of Gauss Points N_{GP} in the sampling window and varying sampling window size R. We considered Adapted Moving Node Approach with the generic component of figure 1a in the configuration $X = 1, Y = 1, L = 3, h = 0.5, \theta = \frac{\pi}{4}, \gamma = 3, \varepsilon = 0.07$ and $dx = 0.07$ for a 50×50 mesh over the domain of X_g.

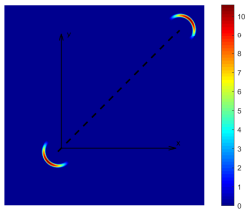

(a) $\frac{\partial W}{\partial L}$

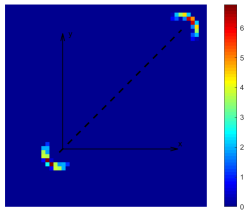

(b) $\frac{\partial \delta}{\partial L}$,$R = \frac{1}{2}dx$, $N_{gp} = 4$

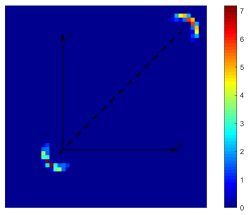

(c) $\frac{\partial \delta}{\partial L}$,$R = \frac{1}{2}dx$, $N_{gp} = 9$

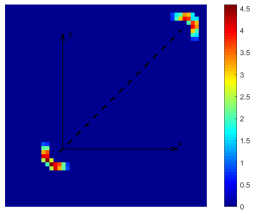

(d) $\frac{\partial \delta}{\partial L}$,$R = dx$, $N_{gp} = 4$

Fig. 28: Sensitivity distribution of W and δ with respect to L for varying number of Gauss Points N_{GP} in the sampling window and varying sampling window size R. We considered Adapted Moving Node Approach with the generic component of figure 1a in the configuration $X = 1, Y = 1, L = 3, h = 0.5, \theta = \frac{\pi}{4}, \gamma = 3, \varepsilon = 0.07$ and $dx = 0.07$ for a 50×50 mesh over the domain of X_g.

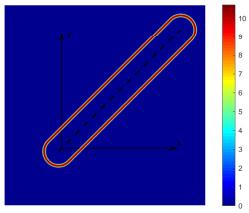

(a) $\frac{\partial W}{\partial h}$

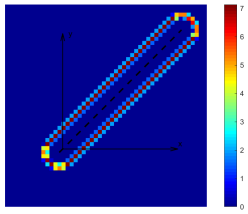

(b) $\frac{\partial \delta}{\partial h}$,$R = \frac{1}{2}dx$, $N_{gp} = 4$

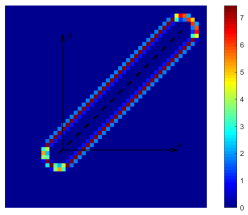

(c) $\frac{\partial \delta}{\partial h}$,$R = \frac{1}{2}dx$, $N_{gp} = 9$

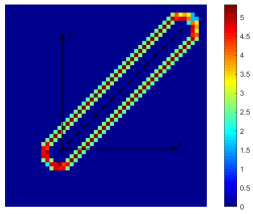

(d) $\frac{\partial \delta}{\partial h}$,$R = dx$, $N_{gp} = 4$

Fig. 29: Sensitivity distribution of W and δ with respect to h for varying number of Gauss Points N_{GP} in the sampling window and varying sampling window size R. We considered Adapted Moving Node Approach with the generic component of figure 1a in the configuration $X = 1, Y = 1, L = 3, h = 0.5, \theta = \frac{\pi}{4}, \gamma = 3, \varepsilon = 0.07$ and $dx = 0.07$ for a 50×50 mesh over the domain of X_g.

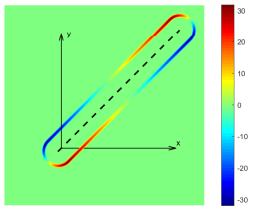

(a) $\frac{\partial W}{\partial \theta}$

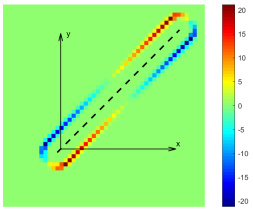

(b) $\frac{\partial \delta}{\partial \theta}$,$R = \frac{1}{2}dx$, $N_{gp} = 4$

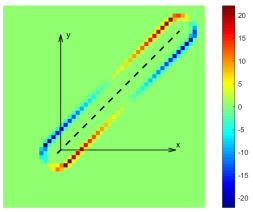

(c) $\frac{\partial \delta}{\partial \theta}$,$R = \frac{1}{2}dx$, $N_{gp} = 9$

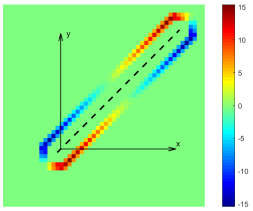

(d) $\frac{\partial \delta}{\partial \theta}$,$R = dx$, $N_{gp} = 4$

Fig. 30: Sensitivity distribution of W and δ with respect to θ for varying number of Gauss Points N_{GP} in the sampling window and varying sampling window size R. We considered Adapted Moving Node Approach with the generic component of figure 1a in the configuration $X = 1, Y = 1, L = 3, h = 0.5, \theta = \frac{\pi}{4}, \gamma = 3, \varepsilon = 0.07$ and $dx = 0.07$ for a 50×50 mesh over the domain of X_g.

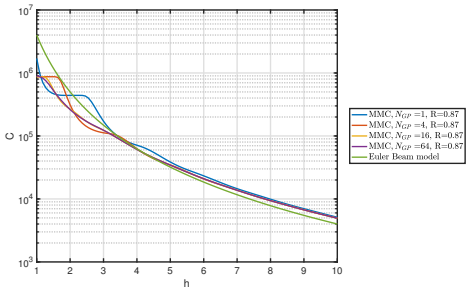

(a) $h - C$ plot for $R = \frac{\sqrt{3}}{2}$, $N_{GP} = \{1, 4, 16, 64\}$

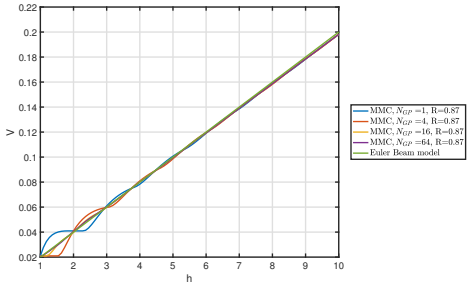

(b) $h - V$ plot for $R = \frac{\sqrt{3}}{2}$, $N_{GP} = \{1, 4, 16, 64\}$

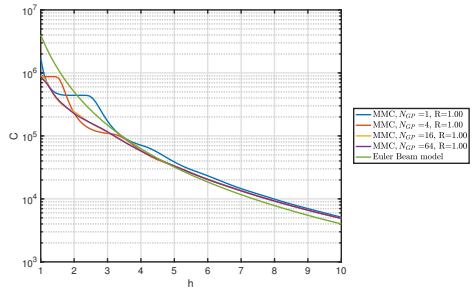

(c) $h - C$ plot for $R = 1$, $N_{GP} = \{1, 4, 16, 64\}$

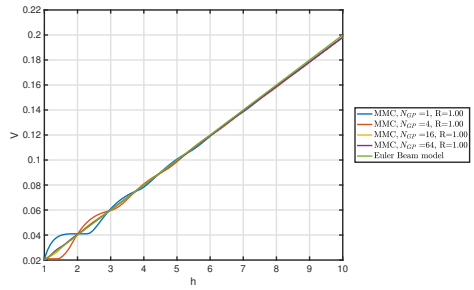

(d) $h - V$ plot for $R = 1$, $N_{GP} = \{1, 4, 16, 64\}$

Fig. 31: Cantilever beam parametric study using the AMMC approach. Effect of the sampling window size R and of the number of Gauss points N_{GP} on the structural compliance and the volume fraction. In each graph we reported in green the true theoretical values based on the analytic beam model.

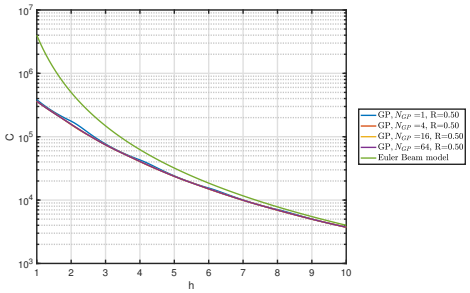

(a) $h - C$ plot for $R = 0.5$, $N_{GP} = \{1, 4, 16, 64\}$

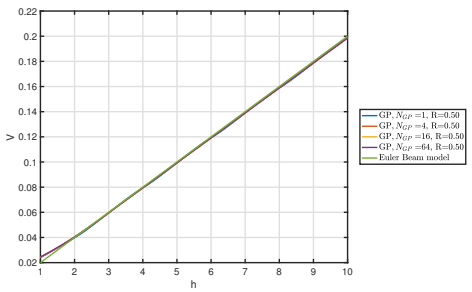

(b) $h - V$ plot for $R = 0.5$, $N_{GP} = \{1, 4, 16, 64\}$

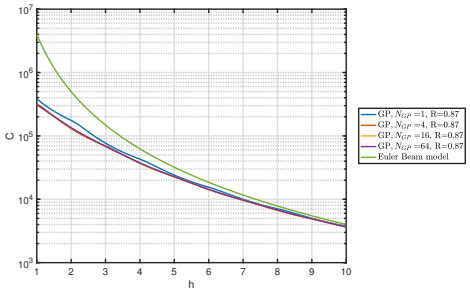

(c) $h - C$ plot for $R = \frac{\sqrt{3}}{2}$, $N_{GP} = \{1, 4, 16, 64\}$

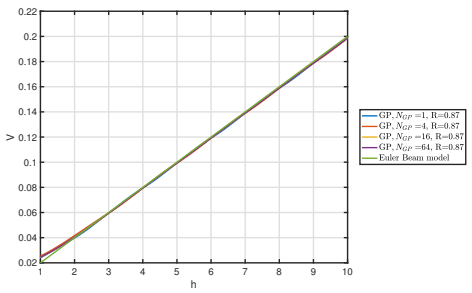

(d) $h - V$ plot for $R = \frac{\sqrt{3}}{2}$, $N_{GP} = \{1, 4, 16, 64\}$

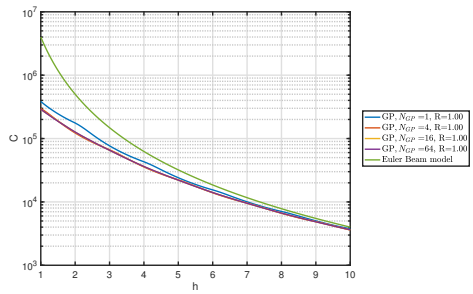

(e) $h-C$ plot for $R = 1$, $N_{GP} = \{1, 4, 16, 64\}$

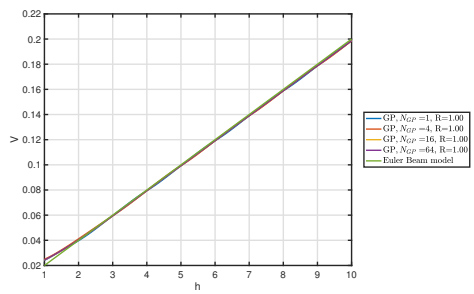

(f) $h-V$ plot for $R = 1$, $N_{GP} = \{1, 4, 16, 64\}$

Fig. 32: Cantilever beam parametric study using AGP method. Effect of the sampling window size R and of the number of Gauss points N_{GP} on the structural compliance and the volume fraction. In each graph we reported in green the true theoretical values based on the analytic beam model.

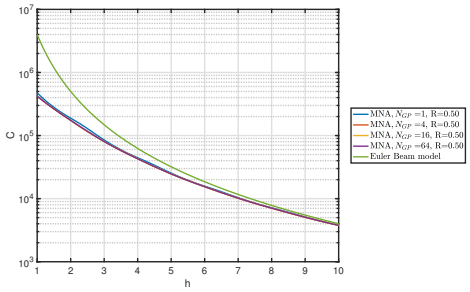

(a) $h - C$ plot for $R = 0.5$, $N_{GP} = \{1, 4, 16, 64\}$

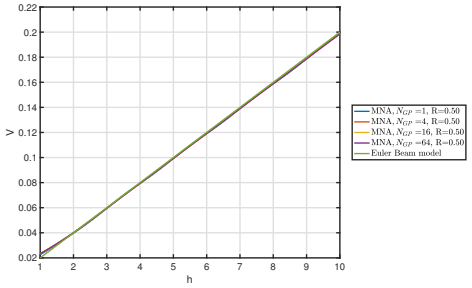

(b) $h - V$ plot for $R = 0.5$, $N_{GP} = \{1, 4, 16, 64\}$

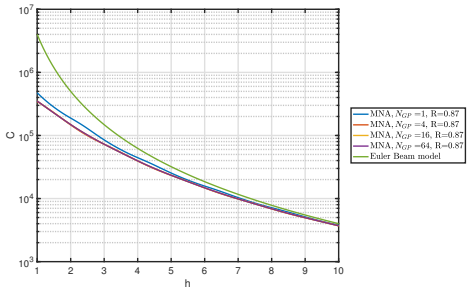

(c) $h - C$ plot for $R = \frac{\sqrt{3}}{2}$, $N_{GP} = \{1, 4, 16, 64\}$

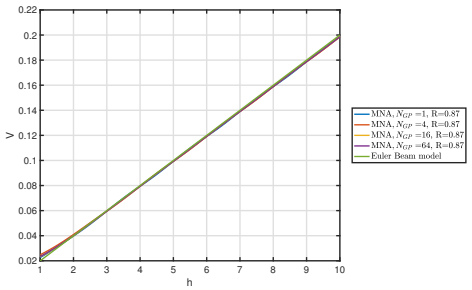

(d) $h - V$ plot for $R = \frac{\sqrt{3}}{2}$, $N_{GP} = \{1, 4, 16, 64\}$

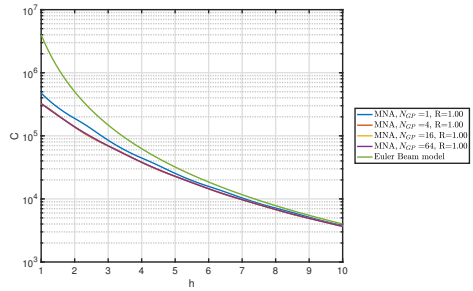

(e) $h - C$ plot for $R = 1$, $N_{GP} = \{1, 4, 16, 64\}$

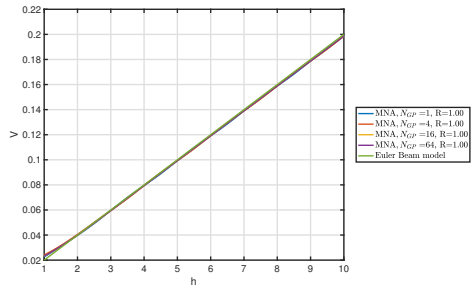

(f) $h - V$ plot for $R = 1$, $N_{GP} = \{1, 4, 16, 64\}$

Fig. 33: Cantilever beam parametric study using the AMNA method. Effect of the sampling window size R and of the number of Gauss points N_{GP} on the structural compliance and the volume fraction. In each graph we reported in green the true theoretical values based on the analytic beam model.

6.3 MMA set-up

In this subsection we provide details of implementations considered for the method of moving asymptotes (MMA, [44]). This approach makes local convex approximations at each iterations of both constraints and objective function. The convexity is adjusted by changing asymptotes' positions during the optimization history. A move limit can also be chosen in order to control the optimization step and avoid divergence. A correct scaling of both design variables and compliance is recommended to avoid numerical issues. Here we propose to re-scale variables and gradients according to:

$$\hat{x}_j = \frac{x_j - l_j}{u_j - l_j} \tag{113}$$

$$\frac{dC}{d\hat{x}_j} = \frac{1}{u_j - l_j}\frac{dC}{dx_j} \tag{114}$$

$$\frac{dV}{d\hat{x}_j} = \frac{1}{u_j - l_j}\frac{dV}{dx_j} \tag{115}$$

where l_j and u_j are the j^{th} - component respectively of the lower bound $\{l\}$ and of upper bound vector $\{u\}$. In order to avoid further MMA numerical issues one can either normalize the compliance dividing C and $\left\{\frac{dC}{d\hat{x}}\right\}$ by a constant C_0 greater than 1 that ensures the compliance and its gradient are small enough. However this way of normalizing introduces the issue of a good choice of C_0, depending on the particular problem studied. To avoid this problem, here we considered the following normalization:

$$\hat{C} = \log\left(1 + C\right) \tag{116}$$

$$\frac{d\hat{C}}{d\hat{x}_j} = \frac{1}{1 + C}\frac{dC}{d\hat{x}_j} \tag{117}$$

$$\tag{118}$$

Note that since $C > 0$, $\log\left(1 + C\right)$ is also greater than 0. This ensures the gradients to be smaller for higher values of C (that is the case of ill connected configurations). In order to avoid MMA divergence due to uncontrolled optimization step length, here we propose a strategy that is similar to the one taken by the globally convergent version of MMA (GCMMA) [45]. In the mmasub.m Matlab function called during the optimization loop we modified the updating of lowmin, lowmax, uppmin and uppmax formula, reducing the value of the coefficients that multiplies each variable range. Accordingly this ensures the control of the optimization step through the overestimation of the problem convexity. In this way MMA behaves more conservatively at each iteration and is less prone to oscillate or to skip local optima[7].

[7] Note that this property can be beneficial or detrimental, depending on the case. Using classic MMA one can either skip worse local optima or better ones in the convergence history.

7 Conflict of Interest

The authors declare that they have no conflict of interest.

Acknowledgements This work has been partially funded by the Association Nationale de la Recherche et de la Technologie (ANRT) through Grant No. CIFRE-2016/0539

References

1. Allaire, G., Jouve, F., Toader, A.M.: Structural optimization using sensitivity analysis and a level-set method. Journal of computational physics **194**(1), 363–393 (2004)
2. Altman, N.S.: An introduction to kernel and nearest-neighbor nonparametric regression. The American Statistician **46**(3), 175–185 (1992)
3. Bell, B., Norato, J., Tortorelli, D.: A geometry projection method for continuum-based topology optimization of structures. In: 12th AIAA Aviation Technology, Integration, and Operations (ATIO) Conference and 14th AIAA/ISSMO Multidisciplinary Analysis and Optimization Conference, vol. 5485 (2012)
4. Bendsøe, M.P.: Optimal shape design as a material distribution problem. Structural optimization **1**(4), 193–202 (1989)
5. Bendsøe, M.P., Kikuchi, N.: Generating optimal topologies in structural design using a homogenization method. Computer methods in applied mechanics and engineering **71**(2), 197–224 (1988)
6. Bendsøe, M.P., Sigmund, O.: Optimization of structural topology, shape, and material, vol. 414. Springer (1995)
7. Borrvall, T.: Topology optimization of elastic continua using restriction. Archives of Computational Methods in Engineering **8**(4), 351–385 (2001)
8. Cai, S., Zhang, W., Zhu, J., Gao, T.: Stress constrained shape and topology optimization with fixed mesh: A b-spline finite cell method combined with level set function. Computer Methods in Applied Mechanics and Engineering **278**, 361–387 (2014)
9. Chen, J., Shapiro, V., Suresh, K., Tsukanov, I.: Shape optimization with topological changes and parametric control. International journal for numerical methods in engineering **71**(3), 313–346 (2007)
10. Chen, S., Wang, M.Y., Liu, A.Q.: Shape feature control in structural topology optimization. Computer-Aided Design **40**(9), 951–962 (2008)
11. Cheng, G., Mei, Y., Wang, X.: A feature-based structural topology optimization method. In: IUTAM Symposium on Topological Design Optimization of Structures, Machines and Materials, pp. 505–514. Springer (2006)
12. Deng, J., Chen, W.: Design for structural flexibility using connected morphable components based topology optimization. Science China Technological Sciences **59**(6), 839–851 (2016)
13. Duysinx, P., Sigmund, O.: New developments in handling stress constraints in optimal material distribution. In: 7th AIAA/USAF/NASA/ISSMO symposium on multidisciplinary analysis and optimization, p. 4906 (1998)
14. Eschenauer, H.A., Kobelev, V.V., Schumacher, A.: Bubble method for topology and shape optimization of structures. Structural optimization **8**(1), 42–51 (1994)

15. Guo, H., Zhao, K., Wang, M.Y.: A new approach for simultaneous shape and topology optimization based on dynamic implicit surface function. Control and Cybernetics **34**, 255–282 (2005)
16. Guo, X., Zhang, W., Zhang, J., Yuan, J.: Explicit structural topology optimization based on moving morphable components (mmc) with curved skeletons. Computer methods in applied mechanics and engineering **310**, 711–748 (2016)
17. Guo, X., Zhang, W., Zhong, W.: Doing topology optimization explicitly and geometricallya new moving morphable components based framework. Journal of Applied Mechanics **81**(8), 081009 (2014)
18. Guo, X., Zhou, J., Zhang, W., Du, Z., Liu, C., Liu, Y.: Self-supporting structure design in additive manufacturing through explicit topology optimization. Computer Methods in Applied Mechanics and Engineering **323**, 27–63 (2017)
19. Hoang, V.N., Jang, G.W.: Topology optimization using moving morphable bars for versatile thickness control. Computer Methods in Applied Mechanics and Engineering **317**, 153–173 (2017)
20. Hou, W., Gai, Y., Zhu, X., Wang, X., Zhao, C., Xu, L., Jiang, K., Hu, P.: Explicit isogeometric topology optimization using moving morphable components. Computer Methods in Applied Mechanics and Engineering **326**, 694–712 (2017)
21. Kazemi, H., Vaziri, A., Norato, J.A.: Topology optimization of structures made of discrete geometric components with different materials. Journal of Mechanical Design **140**(11), 111401 (2018)
22. Kennedy, G.J., Hicken, J.E.: Improved constraint-aggregation methods. Computer Methods in Applied Mechanics and Engineering **289**, 332–354 (2015)
23. Kreisselmeier, G., Steinhauser, R.: Systematic control design by optimizing a vector performance index. In: Computer aided design of control systems, pp. 113–117. Elsevier (1980)
24. Kreissl, S., Maute, K.: Levelset based fluid topology optimization using the extended finite element method. Structural and Multidisciplinary Optimization **46**(3), 311–326 (2012)
25. Lei, X., Liu, C., Du, Z., Zhang, W., Guo, X.: Machine learning-driven real-time topology optimization under moving morphable component-based framework. Journal of Applied Mechanics **86**(1), 011004 (2019)
26. Lin, H.Y., Rayasam, M., Subbarayan, G.: Isocomp: Unified geometric and material composition for optimal topology design. Structural and Multidisciplinary Optimization **51**(3), 687–703 (2015)
27. Liu, C., Du, Z., Zhang, W., Zhu, Y., Guo, X.: Additive manufacturing-oriented design of graded lattice structures through explicit topology optimization. Journal of Applied Mechanics **84**(8), 081008 (2017)
28. Liu, C., Zhu, Y., Sun, Z., Li, D., Du, Z., Zhang, W., Guo, X.: An efficient moving morphable component (mmc)-based approach for multi-resolution topology optimization. arXiv preprint arXiv:1805.02008 (2018)
29. Liu, J., Gaynor, A.T., Chen, S., Kang, Z., Suresh, K., Takezawa, A., Li, L., Kato, J., Tang, J., Wang, C.C.: Current and future trends in topology optimization for additive manufacturing. Structural and Multidisciplinary Optimization pp. 1–27 (2018)
30. Liu, J., Ma, Y.: A survey of manufacturing oriented topology optimization methods. Advances in Engineering Software **100**, 161–175 (2016)
31. Liu, T., Wang, S., Li, B., Gao, L.: A level-set-based topology and shape optimization method for continuum structure under geometric constraints. Structural and Multidisciplinary Optimization **50**(2), 253–273 (2014)
32. Nguyen, V.P., Rabczuk, T., Bordas, S., Duflot, M.: Meshless methods: a review and computer implementation aspects. Mathematics and computers in simulation **79**(3), 763–813 (2008)
33. Norato, J., Bell, B., Tortorelli, D.: A geometry projection method for continuum-based topology optimization with discrete elements. Computer Methods in Applied Mechanics and Engineering **293**, 306–327 (2015)
34. Norato, J., Haber, R., Tortorelli, D., Bendsøe, M.P.: A geometry projection method for shape optimization. International Journal for Numerical Methods in Engineering **60**(14), 2289–2312 (2004)
35. Norato, J.A.: A geometry projection method for the optimal distribution of short fiber reinforcements. In: ASME 2015 International Design Engineering Technical Conferences and Computers and Information in Engineering Conference, pp. V02BT03A010–V02BT03A010. American Society of Mechanical Engineers (2015)
36. Norato, J.A.: Topology optimization with supershapes. Structural and Multidisciplinary Optimization **58**(2), 415–434 (2018)
37. Overvelde, J.T.: The moving node approach in topology optimization. Master's thesis, TU Delft, Delft University of Technology (2012)
38. Qian, Z., Ananthasuresh, G.: Optimal embedding of rigid objects in the topology design of structures. Mechanics Based Design of Structures and Machines **32**(2), 165–193 (2004)
39. Saxena, A.: Are circular shaped masks adequate in adaptive mask overlay topology synthesis method? Journal of Mechanical Design **133**(1), 011001 (2011)
40. Seo, Y.D., Kim, H.J., Youn, S.K.: Isogeometric topology optimization using trimmed spline surfaces. Computer Methods in Applied Mechanics and Engineering **199**(49-52), 3270–3296 (2010)
41. Sigmund, O.: Design of materials structures using topology optimization. Ph.D. thesis, Department of Solid Mechanics, Technical University of Denmark (1994)
42. Smola, A.J., Schölkopf, B.: A tutorial on support vector regression. Statistics and computing **14**(3), 199–222 (2004)
43. Sun, J., Tian, Q., Hu, H.: Topology optimization of a three-dimensional flexible multibody system via moving morphable components. Journal of Computational and Nonlinear Dynamics **13**(2), 021010 (2018)
44. Svanberg, K.: The method of moving asymptotesa new method for structural optimization. International journal for numerical methods in engineering **24**(2), 359–373 (1987)
45. Svanberg, K.: A class of globally convergent optimization methods based on conservative convex separable approximations. SIAM journal on optimization **12**(2), 555–573 (2002)
46. Svanberg, K.: Some modelling aspects for the matlab implementation of mma. KTH Royal Institute of Technology, Stockholm (2004)
47. Takalloozadeh, M., Yoon, G.H.: Implementation of topological derivative in the moving morphable components approach. Finite Elements in Analysis and Design **134**, 16–26 (2017)
48. Van Miegroet, L., Duysinx, P.: Stress concentration minimization of 2d filets using x-fem and level set description.

Structural and Multidisciplinary Optimization **33**(4-5), 425–438 (2007)
49. Wang, F., Jensen, J.S., Sigmund, O.: High-performance slow light photonic crystal waveguides with topology optimized or circular-hole based material layouts. Photonics and Nanostructures-Fundamentals and Applications **10**(4), 378–388 (2012)
50. Wang, M.Y., Wang, X., Guo, D.: A level set method for structural topology optimization. Computer methods in applied mechanics and engineering **192**(1), 227–246 (2003)
51. Wang, X., Long, K., Hoang, V.N., Hu, P.: An explicit optimization model for integrated layout design of planar multi-component systems using moving morphable bars. Computer Methods in Applied Mechanics and Engineering **342**, 46–70 (2018)
52. Watts, S., Tortorelli, D.A.: A geometric projection method for designing three-dimensional open lattices with inverse homogenization. International Journal for Numerical Methods in Engineering **112**(11), 1564–1588 (2017)
53. Wei, P., Wang, M.Y., Xing, X.: A study on x-fem in continuum structural optimization using a level set model. Computer-Aided Design **42**(8), 708–719 (2010)
54. Xia, L., Xia, Q., Huang, X., Xie, Y.M.: Bi-directional evolutionary structural optimization on advanced structures and materials: a comprehensive review. Archives of Computational Methods in Engineering **25**(2), 437–478 (2018)
55. Xia, L., Zhu, J., Zhang, W.: Sensitivity analysis with the modified heaviside function for the optimal layout design of multi-component systems. Computer Methods in Applied Mechanics and Engineering **241**, 142–154 (2012)
56. Xie, Y., Steven, G.P.: A simple evolutionary procedure for structural optimization. Computers & structures **49**(5), 885–896 (1993)
57. Xue, R., Liu, C., Zhang, W., Zhu, Y., Tang, S., Du, Z., Guo, X.: Explicit structural topology optimization under finite deformation via moving morphable void (mmv) approach. Computer Methods in Applied Mechanics and Engineering **344**, 798–818 (2019)
58. Zhang, S., Gain, A.L., Norato, J.A.: Stress-based topology optimization with discrete geometric components. Computer Methods in Applied Mechanics and Engineering **325**, 1–21 (2017)
59. Zhang, S., Gain, A.L., Norato, J.A.: A geometry projection method for the topology optimization of curved plate structures with placement bounds. International Journal for Numerical Methods in Engineering **114**(2), 128–146 (2018)
60. Zhang, S., Norato, J.A.: Optimal design of panel reinforcements with ribs made of plates. Journal of Mechanical Design **139**(8), 081403 (2017)
61. Zhang, S., Norato, J.A.: Finding better local optima in topology optimization via tunneling. In: ASME 2018 International Design Engineering Technical Conferences and Computers and Information in Engineering Conference, pp. V02BT03A014–V02BT03A014. American Society of Mechanical Engineers (2018)
62. Zhang, S., Norato, J.A., Gain, A.L., Lyu, N.: A geometry projection method for the topology optimization of plate structures. Structural and Multidisciplinary Optimization **54**(5), 1173–1190 (2016)
63. Zhang, W., Chen, J., Zhu, X., Zhou, J., Xue, D., Lei, X., Guo, X.: Explicit three dimensional topology optimization via moving morphable void (mmv) approach. Computer Methods in Applied Mechanics and Engineering **322**, 590–614 (2017)
64. Zhang, W., Li, D., Yuan, J., Song, J., Guo, X.: A new three-dimensional topology optimization method based on moving morphable components (mmcs). Computational Mechanics **59**(4), 647–665 (2017)
65. Zhang, W., Li, D., Zhang, J., Guo, X.: Minimum length scale control in structural topology optimization based on the moving morphable components (mmc) approach. Computer Methods in Applied Mechanics and Engineering **311**, 327–355 (2016)
66. Zhang, W., Li, D., Zhou, J., Du, Z., Li, B., Guo, X.: A moving morphable void (mmv)-based explicit approach for topology optimization considering stress constraints. Computer Methods in Applied Mechanics and Engineering **334**, 381–413 (2018)
67. Zhang, W., Liu, Y., Du, Z., Zhu, Y., Guo, X.: A moving morphable component based topology optimization approach for rib-stiffened structures considering buckling constraints. Journal of Mechanical Design **140**(11), 111404 (2018)
68. Zhang, W., Song, J., Zhou, J., Du, Z., Zhu, Y., Sun, Z., Guo, X.: Topology optimization with multiple materials via moving morphable component (mmc) method. International Journal for Numerical Methods in Engineering **113**(11), 1653–1675 (2018)
69. Zhang, W., Xia, L., Zhu, J., Zhang, Q.: Some recent advances in the integrated layout design of multicomponent systems. Journal of Mechanical Design **133**(10), 104503 (2011)
70. Zhang, W., Yang, W., Zhou, J., Li, D., Guo, X.: Structural topology optimization through explicit boundary evolution. Journal of Applied Mechanics **84**(1), 011011 (2017)
71. Zhang, W., Yuan, J., Zhang, J., Guo, X.: A new topology optimization approach based on moving morphable components (mmc) and the ersatz material model. Structural and Multidisciplinary Optimization **53**(6), 1243–1260 (2016)
72. Zhang, W., Zhang, J., Guo, X.: Lagrangian description based topology optimizationa revival of shape optimization. Journal of Applied Mechanics **83**(4), 041010 (2016)
73. Zhang, W., Zhong, W., Guo, X.: Explicit layout control in optimal design of structural systems with multiple embedding components. Computer Methods in Applied Mechanics and Engineering **290**, 290–313 (2015)
74. Zhang, W., Zhou, J., Zhu, Y., Guo, X.: Structural complexity control in topology optimization via moving morphable component (mmc) approach. Structural and Multidisciplinary Optimization **56**(3), 535–552 (2017)
75. Zhang, W., Zhou, Y., Zhu, J.: A comprehensive study of feature definitions with solids and voids for topology optimization. Computer Methods in Applied Mechanics and Engineering **325**, 289–313 (2017)
76. Zhou, M., Rozvany, G.: The coc algorithm, part ii: topological, geometrical and generalized shape optimization. Computer Methods in Applied Mechanics and Engineering **89**(1-3), 309–336 (1991)
77. Zhou, M., Wang, M.Y.: Engineering feature design for level set based structural optimization. Computer-Aided Design **45**(12), 1524–1537 (2013)
78. Zhou, Y., Zhang, W., Zhu, J., Xu, Z.: Feature-driven topology optimization method with signed distance function. Computer Methods in Applied Mechanics and Engineering **310**, 1–32 (2016)

79. Zhu, B., Chen, Q., Wang, R., Zhang, X.: Structural topology optimization using a moving morphable component-based method considering geometrical nonlinearity. Journal of Mechanical Design **140**(8), 081403 (2018)
80. Zhu, J., Zhang, W., Beckers, P., Chen, Y., Guo, Z.: Simultaneous design of components layout and supporting structures using coupled shape and topology optimization technique. Structural and Multidisciplinary Optimization **36**(1), 29–41 (2008)
81. Zhu, J.H., Zhang, W.H., Xia, L.: Topology optimization in aircraft and aerospace structures design. Archives of Computational Methods in Engineering **23**(4), 595–622 (2016)